1 **The Structural Basis for SARM1 Inhibition and Activation Under Energetic Stress**

2

3 **Michael Sporny[1,9], Julia Guez-Haddad[1,9], Tami Khazma[1,9], Avraham Yaron[2], Moshe**

4 **Dessau[3], Yoel Shkolnisky[4], Carsten Mim[5,+], Michail N. Isupov[6,+], Ran Zalk[7,+], Michael**

5 **Hons[8,+], and Yarden Opatowsky[1*]**

6 [1]The Mina & Everard Goodman Faculty of Life Sciences, Bar-Ilan University,

7 Ramat-Gan, Israel

8 [2]Department of Biomolecular Sciences, Weizmann Institute of Science, Rehovot, Israel

9 [3]Azrieli Faculty of Medicine, Bar Ilan University, Safed, Israel

10 [4]Department of Applied Mathematics, School of Mathematical Sciences, Tel-Aviv University,

11 Tel-Aviv, Israel

12 [5]Royal Technical Institute (KTH), Dept. For Biomedical Engineering and Health Systems,

13 Stockholm, Sweden

14 [6]Biosciences, University of Exeter, England

15 [7]National Institute for Biotechnology in the Negev, Ben-Gurion University of the Negev, Beer-

16 Sheva, Israel

17 [8]European Molecular Biology Laboratory, Grenoble, France

18 [9]Co-first authors

19 [+]These authors have contributed equally to this work

20

21 Address correspondence to Yarden Opatowsky, The Mina & Everard Goodman Faculty of

22 Life Sciences, Bar-Ilan University, Ramat-Gan 5290002, Israel.

23 Tel: +972-3-5318330, +972-54-2203403; Fax: +972-3-7369231;

24 E-mail: yarden.opatowsky@biu.ac.il

25

26

27 **Abstract**

28

29 SARM1 an executor of axonal degeneration, displays NADase activity that depletes the key
30 cellular metabolite, NAD+, in response to nerve injury. The basis of SARM1 inhibition, and its
31 activation under stress conditions are still unknown. Here, we present cryo-EM maps of SARM1
32 at 2.9 and 2.7 Å resolution. These indicate that SARM1 homo-octamer avoids premature
33 activation by assuming a packed conformation, with ordered inner and peripheral rings, that
34 prevents dimerization and activation of the catalytic domains. This inactive conformation is
35 stabilized by binding of SARM1's own substrate NAD+ in an allosteric location, away from the
36 catalytic sites. This model was validated by mutagenesis of the allosteric site, which led to
37 constitutively active SARM1. We propose that the reduction of cellular NAD+ concentration
38 contributes to the disassembly of SARM1's peripheral ring, which allows formation of active
39 NADase domain dimers, thereby further depleting NAD+ to cause an energetic catastrophe and
40 cell death.

41

42

43 Keywords: SARM1; cell death; Cryo-EM; structural biology; NAD+ metabolism; substrate
44 inhibition

45

52

Introduction

SARM1 (sterile α and HEAT/armadillo motif–containing protein (Mink et al., 2001)) was first discovered as a negative regulator of TRIF (TIR domain–containing adaptor inducing interferon-β) in TLR (Toll-like receptor) signaling (Carty et al., 2006). SARM1 was later shown to promote neuronal death by oxygen and glucose deprivation (Kim et al., 2007) and viral infections (Hou et al., 2013; Mukherjee et al., 2013; Sundaramoorthy et al., 2020; Uccellini et al., 2020), while also having a protective role against bacterial and fungal infections in *C. elegans* (Couillault et al., 2004; Liberati et al., 2004). Subsequently, studies have demonstrated that SARM1 is also a key part of a highly conserved axonal death pathway that is activated by nerve injury (Gerdts et al., 2013; Osterloh et al., 2012). Notably, SARM1 deficiency confers protection against axonal degeneration in several models of neurodegenerative conditions (Kim et al., 2007; Ko et al., 2020; Ozaki et al., 2020; Uccellini et al., 2020), making SARM1 a compelling drug target to protect axons in a variety of axonopathies (Krauss et al., 2020; Loring et al., 2020). The domain composition of SARM1 includes an N-terminal peptide, an ARM-repeats region, two SAM and one TIR domain (Figure 1A, Figure 1 - Figure supplement 1), which mediate mitochondria targeting (Panneerselvam et al., 2012), auto-inhibition (Chuang and Bargmann, 2005; Summers et al., 2016), oligomerization (Gerdts et al., 2013), and NADase activity (Gerdts et al., 2015), respectively.

Amino acid substitutions (E642A or E596K) at the TIR domain's active site abolish the NADase activity *in vitro* and inactivates SARM1 pro-degenerative activity (Essuman et al., 2017; Geisler et al., 2019; Horsefield et al., 2019), thereby linking SARM1's role in axonal degeneration with its NADase activity. The enzymatic activity requires a high local concentration of the TIR domains, as demonstrated by forced dimerization of TIR, which resulted in NAD+ hydrolysis and neuronal cell death (Gerdts et al., 2015; Gerdts et al., 2016). Also, the deletion of the ARM domain in SARM1, which interacts directly with TIR (Summers et al., 2016), renders the 'delARM' construct constitutively active and leads to rapid cell death (Gerdts et al., 2013; Sporny et al., 2019). How SAM domains cause TIR crowding became clearer in our recent report (Sporny et al., 2019), where we showed that both hSARM1 (human SARM1) and the isolated tandem SAM[1-2] domains form octamers in solution. In this study, we used negative stain electron microscopy analysis of hSARM1 and determined the crystal structure (as did others (Horsefield et al., 2019)) of the SAM[1-2] domains - both of which revealed an octameric ring arrangement.

These findings imply that hSARM1 is kept auto-inhibited by the ARM domain in homeostasis, and gains NADase activity upon stress conditions through: the infliction of injury (axotomy (Osterloh et al., 2012)), oxidation (mitochondria depolarization (Murata et al., 2013); oxidizing agents (Summers et al., 2014)), metabolic conditions (depletion of NAD+ (Gilley et al., 2015)), or toxins (chemotherapy drugs (Geisler et al., 2016)). Whether and how all or some of these insults converge to induce SARM1 activation is still not completely understood. In this regard, little is

90 known about the direct molecular triggers of SARM1 in cells, besides the potential involvement of
91 nicotinamide mononucleotide (NMN) (Bratkowski et al., 2020; Liu et al., 2018a; Zhao et al., 2019)
92 and Ser-548 phosphorylation by JNK (Murata et al., 2018) in promoting the NADase activity of
93 SARM1. Here we present structural data and complementary biochemical assays, to show that
94 SARM1 is kept inactive through a 'substrate inhibition' mechanism, where the high concentration
95 of NAD+ stabilizes the tightly packed, inhibited conformation of the protein. In this way, SARM1
96 activation is triggered by a decrease in the concentration of a cellular metabolite - NAD+, rather
97 than depend on the introduction of an activating factor.
98

99 **Results**
100 **Cryo-EM visualization of purified hSARM1**
101 For cryo-EM imaging, we generated a near-intact hSARM1 construct, that lacks the N-terminal
102 mitochondrial localization signal ([26]ERL…GPT[724]) and has a point mutant in the NADase catalytic
103 site (E642Q). The resulting construct was expressed in mammalian cell culture and isolated to
104 homogeneity using consecutive metal chelate and size exclusion chromatography steps. For
105 cellular and *in vitro* activity assays we expressed and isolated hSARM1[w.t.] ([26]ERL…GPT[724])
106 without the E642 mutation (Figure 1B, Figure 1 - Figure supplement 1), although with lower
107 yields. We first collected cryo-EM images of the purified hSARM1[E642Q]. 2D classification (Figure
108 1C) and 3D reconstruction (Figure 1D, Table 1) revealed an octamer ring assembly with clearly
109 visible inner ring, which is attributed to the tandem SAM domains. Only a minor fraction of the
110 particles (~20%) shows the presence of a (partial) peripheral ring composed by the ARM and TIR
111 domains. Cryo-EM analysis of the isolated SAM[1-2] domains (Figure 1D), and docking of the
112 crystal structure of the SAM[1-2] octamer (PDB code 6QWV) into the 3D maps demonstrates that
113 indeed, the ARM and TIR domains are largely missing from this reconstruction, implying a
114 disordered peripheral ring in ~80% of the particles. Exploring different buffers, pH and salt
115 conditions, addition of various detergents, as well as variations in cryo-EM grid preparation (e.g.
116 ice thickness) did not affect the visibility of the octamer peripheral ring considerably.
117 These results are inconsistent with our previous analysis, where we used low resolution negative
118 stain EM visualization and 2D classification of hSARM1[E642Q] that showed fully assembled inner
119 and outer ring structures (Figure 1C) (Sporny et al., 2019). We thought, that a glycerol-gradient
120 fixation step (GraFix (Kastner et al., 2008)) that involves ultra-centrifugation of the protein sample
121 through a glycerol + glutaraldehyde cross-linker gradients, which was applied before the negative
122 stain - but not before the cryo-EM sample preparations - might be the cause for the difference
123 between the two imaging conditions. We therefore pursued cryo-EM data collection of GraFix-ed
124 hSARM1[E642Q] after dilution of the glycerol from 18% (which severely diminishes protein contrast in
125 cryo-EM) to 2.5%.
126

2.88 Å resolution structure of a fully assembled compact hSARM1 GraFix-ed octamer

We carried out 2D classification (Figure 2A), and 3D reconstruction and refinement (Figure 2B-D, Table 1) of the GraFix-ed hSARM1^{E642Q} to an overall resolution of 2.88 Å (applying 8-fold symmetry). The hSARM1^{E642Q} octamer is 203 Å in diameter and 80 Å thick (Figure 2 - Figure supplement 1A). The SAM$^{1-2}$ domains' inner ring is the best resolved part of the map, to which the high-resolution crystal structure (PDB code 6QWV) was fitted with minute adjustments. The TIR domains are the least defined part of the density map. Some parts of the TIR domain reach a local resolution of 6.5 Å (Figure 2 - Figure supplement 2A), and therefore not revealing side chain positions. However, the availability of high-resolution crystal structures of isolated hSARM1 TIR (PDB codes 6O0R, 6O0U (Horsefield et al., 2019)) allowed their docking into the well resolved secondary structure elements in the map with very high confidence. The ARM domains show intermediate map quality, with well resolved secondary structures and bulky sidechains. This allowed the building of a de-novo atomic model for the entire ARM, as no high-resolution structure or homology models of SARM1's ARM are available. The entire atomic model is comprised of residues 56-700 (Figure 1 - Figure supplement 1), with an internal break at the linker that connects SAM^2 to the TIR domain. The structural analyses of the SAM domains and the SAM octamer ring assembly, as well as the atomic details of the TIR domain, are described in our previous study, and by others (Horsefield et al., 2019; Sporny et al., 2019). The cryo-EM structure of the ARM domain reveals a closed crescent-shaped region, composed of seven three-helix ARM repeats spanning residues 60-400 (Figure 2 - Figure supplement 1B). The ARM topology is split into two interacting parts, designated ARM^1 (res. 60-303 with five ARM repeats) and ARM^2 (res. 322-400 with two ARM repeats) (Figure 1 - Figure supplement 1). The main ARM^1 - ARM^2 interaction interface is hydrophobic and involves helices α14 and 16 of ARM^1 and helices α1, 2 and 3 of ARM^2. ARM^1 and ARM^2 are also interacting at the crescent 'horns' through the ARM^1 α2-α3 loop with the loop that connects ARM^1 with ARM^2 (res. 305-320). In the hSARM1 compact octamer, each ARM is directly connected via a linker (res. 400-404) to a SAM^1 domain. Also, each ARM is engaged in several non-covalent interactions with the same-chain SAM and with the clockwise neighboring SAM, when assuming a top view of the structure (Figure 2B-D). Although neighboring ARM domains are closely packed, direct interactions between them seem to be limited, engaging a short segment of ARM^1 α9 with the α4-α5 loop of ARM^2 of the neighboring chain. Additional ARM-ARM interactions are indirect, mediated by the TIR domains. Each TIR binds the ARM ring via two sites, designated the 'primary' and 'secondary' TIR docking sites (Figure 3A). The 'primary' is larger and engages the TIR helix αA and the EE loop with the ARM^1 α10, α10-11 loop and α13. The 'secondary' TIR docking site is smaller and involves the TIR BB loop and helix α7 of the counter-clockwise ARM^1 domain (Figure 1 - Figure supplement 1).

163 Very recently, (Bratkowski et al., 2020) have reported a 3.3 Å cryo-EM structure of hSARM1[50-724].

164 Except for a residue registry shift throughout the ARM[1] α1-4 and a minor one at the ARM[1]-ARM[2]

165 loop, their structure is largely similar to our 2.88 Å GraFix-ed structure. While we have used the

166 GraFix pre-treatment to coerce the compact two-ring conformation, it seems that Bratkowski et.

167 al. employed a different strategy by selectively using a small subset (5.6%) of the initial picked

168 particles to reconstruct their map. We assume that this was done to cope with the particle

169 heterogeneity of purified SARM1. An obstacle we have encountered as well, where we observed

170 that ~80% of the particles have a disordered outer ring.

171

172 **The compact conformation of hSARM1 is inhibited for NADase activity**

173 The GraFix-ed cryo-EM structure revealed a domain organization where the catalytic TIR

174 subunits are separated from each other by docking onto the ARM peripheral ring. This assembly

175 is dependent on the coupling of each TIR with two neighboring ARM domains (Figure 3A). Since

176 the NADase activity requires close proximity of several of TIR domains (Bratkowski et al., 2020;

177 Gerdts et al., 2015; Gerdts et al., 2016), and possibly homo-dimerization (Horsefield et al., 2019),

178 we considered that the cryo-EM structure represents an inhibited conformation of SARM1, in

179 which the TIR domains cannot form compact dimers and catabolize NAD+. To test this

180 hypothesis, we aimed to weaken TIR docking to allow their nearing and subsequent NAD+

181 catalysis. To this end we designed amino acid substitutions at the ARM's primary TIR docking

182 site without compromising the protein's structural integrity – particularly that of the TIR domain

183 (Figure 3A). Two pairs of mutations - RR216-7EE of ARM[1] helix α10, and FP255-6RR of ARM[1]

184 helix α13 (Figure 3C, Figure 1 - Figure supplement 1) were introduced, as well as the double

185 mutant RR216-7EE/FP255-6RR. These constructs were transiently expressed in HEK-293T cells.

186 The effect of these constructs on NAD+ levels and cell viability were monitored using a previously

187 established resazurin fluorescence assay (Essuman et al., 2018; Gerdts et al., 2013; Sporny et

188 al., 2019). The results (Figure 3C) show a rapid decrease in cellular NAD+ levels and 50% cell

189 death within 24 hours after transfection of the FP255-6RR and double mutant. This toxicity level

190 is similar to that of a hSARM1 construct missing the entire ARM domain 'delARM' (res. 409–724)

191 (Figure 3C), proven to be toxic in neurons and HEK293 cells (Gerdts et al., 2013; Sporny et al.,

192 2019). This toxic effect was attributed to the removal of auto-inhibitory constraints imposed by the

193 ARM domain. The RR216-7EE mutation has a weaker effect, probably due to the position of

194 these amino acid residues at the margin of the TIR-ARM interface.

195 In conclusion, we found that hSARM1 inhibition requires ARM-TIR interaction through the

196 'primary TIR docking site'. This conclusion is supported by other recently published reports

197 (Bratkowski et al., 2020; Jiang et al., 2020). We further calculated the surface conservation

198 scores of SARM1 orthologs. The scores were color coded and plotted on the molecular surface of

199 hSARM1 using the Consurf server (Figure 3B)(Ashkenazy et al., 2016). The surface-exposed

200 residues reveal a high level of conservation on both the ARM and TIR domain binding interface.

201 This indicates the biological importance of the interface and a possible conservation of its

202 function in auto-inhibition among species. It was previously suggested, that auto-inhibition of

203 SARM1 is maintained by keeping SARM1 as a monomer, and that upon activation SARM1

204 assembles into a multimer (Figley and DiAntonio, 2020), very much like other apoptotic

205 complexes. Our results show otherwise, and explain how hSARM1 avoids premature activation

206 even as a pre-formed octamer, while kept poised for rapid activation and response.

207

208 **Isolated hSARM1 is NADase active *in vitro* and inhibited by glycerol**

209 As it became clear that the compact two-ring structure is inhibited for NADase activity, we

210 considered whether the purified hSARM1, that was not subjected to GraFix, and predominantly

211 presents just the inner SAM ring in cryo-EM 2D averaging and 3D reconstruction (Figure 1C,D),

212 is active *in vitro*. Using a resazurin fluorescence assay modified for an *in vitro* application, we

213 measured the rate of NAD+ consumption by hSARM1[w.t.] in a series of NAD+ concentrations and

214 determined a *Km* of 28±4 µM, with *Vmax* of 9±0.3 µM/min and *Kcat* of 46.49 1/min (Figure 3D).

215 These kinetic parameters are remarkably similar to a published *Km* of 24 µM (Essuman et al.,

216 2017) – especially when considering that the quoted study used an isolated TIR domain fused to

217 artificial dimerizing and aggregating agents, while we used the near-intact protein.

218 It was previously discovered that nicotinamide mononucleotide (NMN) levels rises after axonal

219 injury, and that exogenous increase of NMN induces degeneration (Di Stefano et al., 2015).

220 Moreover, a membrane-permeable NMN analogue activates SARM1 in cultured cells, leading to

221 their death (Liu et al., 2018a; Zhao et al., 2019). We therefore measured the effect of NMN

222 supplement on the NADase activity of purified hSARM1 and found a moderate 30% increase in

223 activity with 1 mM NMN, but none at a lower concentration of 200 µM (Figure 3E). This

224 demonstrates that the purified hSARM1 is mostly NADase active, even without NMN supplement,

225 supporting the idea of a predominantly open conformation as seen in cryo-EM (Figure 1C,D).

226 Next, we examined what confines the GraFix-ed hSARM1 into the compact inhibited

227 conformation (Figure 2), and measured the *in vitro* NADase activity in the presence of glycerol

228 (Figure 3F). We found that glycerol reduces hSARM1 NADase activity in a concentration-

229 dependent manner, reaching 72% inhibition at 15% glycerol. In the GraFix preparation, we

230 extracted hSARM1 from the gradient after it migrated to approximately 18% glycerol

231 concentration. This is the position we used to image SARM1 in its inhibited compact

232 conformation. It seems likely, that this conformation is maintained after glycerol is removed, due

233 to glutaraldehyde crosslinking which preserves the compact structure.

234

235 **NAD+ substrate inhibition of hSARM1**

236 Our results show that hSARM1 NADase activity is suppressed in cell culture, but much less so *in*
237 *vitro* after being isolated. This prompted us to hypothesize that in the course of purification from
238 the cytosolic fraction, hSARM1 loses a low-affinity cellular factor, responsible for inhibiting it in the
239 cellular environment. SARM1 was previously shown to be activated in cell culture in response to
240 metabolic, toxic and oxidative stressors. We reasoned that the hypothesized inhibitory factor is a
241 small molecule that is depleted under cellular stress conditions and thus, the inhibition of
242 hSARM1 is released. To follow through on this hypothesis, we tested the impact of several small
243 molecules, which are associated with the cell's energetic state, with two *in vitro* parameters:
244 hSARM1 NADase activity, and structural conformation (visualized by cryo-EM). For instance, we
245 already established that glycerol meets these two criteria, as it imposes hSARM1 compact
246 conformation (Figure 2) and reduces NADase activity (Figure 3F). Curiously, glycerol was found
247 to occupy the active site of the hSARM1 TIR domain in a crystal structure (PDB code 6O0R
248 (Horsefield et al., 2019)), directly linking structural data with enzymatic inhibition. However, the
249 glycerol concentrations in which these *in vitro* experiments were conducted were very high (15-
250 18% for the NADase activity assay and cryo-EM, and 25-30% in the X-ray crystal structure), i.e.
251 2-4 M, which is considerably higher than the estimated sub 1 mM concentrations of intracellular
252 physiological glycerol (Li and Lin, 1983). Next, we considered ATP as a fit candidate to inhibit
253 hSARM1, because ATP is the main energetic compound, with cellular concentrations between 1-
254 10 mM, which is depleted prior to cell death and axonal degeneration. Indeed, we found that ATP
255 inhibits the NADase activity of hSARM1 in a dose-dependent manner (Figure 4A). However, it did
256 not affect hSARM1 conformation as observed by 2D classification (Figure 4B). Therefore, it is
257 possible that ATP inhibits hSARM1 through the TIR domain's active site.
258 It was reported that NAD+ levels drop in response to axon injury (Coleman and Hoke, 2020).
259 Also, the ablation of the cytosolic NAD+ synthesizing enzymes NMNAT1 and 2 decreases
260 cytoplasmic NAD+, and induces SARM1 activation (Gilley et al., 2015; Sasaki et al., 2016).
261 Therefore, we postulated that it is the high physiological concentration of NAD+ itself, that may
262 inhibit hSARM1 through 'substrate inhibition' - a general mechanism regulating the activity of
263 many enzymes (Reed et al., 2010). Cryo-EM images show that adding 5mM NAD+ to hSARM1
264 has a dramatic effect: >80% of the particles show the two-ring, compact conformation – in
265 contrast to the <20% found in the absence of NAD+ (Figure 4B,C). To measure NAD+ substrate
266 inhibition of hSARM1, we used a fluorescent assay with a wide concentration range of the NAD+
267 analog, etheno-NAD (eNAD) (mixed 1:10 mol/mol with regular NAD+). eNAD fluoresces upon
268 hydrolysis (ex. λ = 330 nm, em. λ = 405 nm). The results showed a bell-shape curve (Figure 4D)
269 with the highest rate of hydrolysis at 100µM NAD+ and a steady decrease in rate thereafter (at
270 the higher concentrations). In addition, we used a direct reverse-phase HPLC monitoring of
271 NAD+ consumption by hSARM1 compared with commercially available porcine brain NADase.

272 While the rate of hydrolysis of porcine NADase was maintained between 50μM and 2mM NAD+,
273 hSARM1 was almost completely inhibited at 2mM NAD+ (Figure 4E).
274

275 **2.7 Å resolution structure of NAD+ induced hSARM1 compact octamer**
276 Following evidence for NAD+ substrate inhibition of hSARM1 by cryo-EM 2D classification
277 (Figure 4B,C) and enzymatic (Figure 4D,E) assays, we pursued a 3D structure determination of
278 hSARM1 complexed with NAD+ at inhibiting concentrations. hSARM1, supplemented by 5mM
279 NAD+, was imaged, reconstructed and refined to 2.7 Å resolution (Figure 5A), resulting in an
280 excellent map (Figure 5 and Figure 5 - Figure supplement 1). The structure was largely identical
281 to the GraFix-ed structure, further substantiating the validity of the latter (Figure 5B). Few
282 structural differences can be observed between the NAD+ supplemented density map and that of
283 the GraFix-ed hSARM1. The first difference is a 5Å shift in the position of the distal part of the
284 TIR domain, and the second is a rearrangement of the secondary structure at the region of the
285 'crescent horns', where the tips of ARM[1] and ARM[2] touch (Figure 5C, Figure 5 - Figure
286 supplements 1 and 2A,B). In the same region, designated hereafter 'ARM allosteric site', an
287 extra-density in the NAD+ supplemented map reveals the binding site of one NAD+ molecule,
288 providing clear atomic details (Figure 5C, right panel). To probe into the function of the ARM
289 allosteric site, we introduced point mutations, targeting three structural elements surrounding the
290 NAD+ density. These elements were: ARM[1] α2; ARM[1] α5-6 loop; and the ARM[1]-ARM[2] loop
291 (Figure 5C,D, Figure 5 - Figure supplement 2). As a control, we introduced two other mutations in
292 sites that we do not consider to be involved in hSARM1 inhibition or activation. We hypothesized
293 that NAD+ binding at the ARM allosteric site stabilizes the ARM conformation by interacting with
294 both ARM[1] and ARM[2], thereby promoting the hSARM1 compact auto-inhibited structure.
295 Therefore, mutations in the allosteric site, that interfere with NAD+ binding, would diminish auto-
296 inhibition and allow hSARM1 activity in cell culture. Indeed, we found that two separate mutations
297 in the ARM[1] α5-6 loop (L152A, and R157E) and one in the opposite ARM[1]-ARM[2] loop (R322E)
298 had a dramatic effect on hSARM1 activity, promoting cell death levels comparable to those
299 induced by the 'delARM' 'constitutively active' construct, which is missing the entire ARM domain
300 (Figure 5D). Two mutations (D314A and Q320A), that are also located at the ARM[1]-ARM[2] loop
301 but their side chains positioned away from the NAD+ molecule, did not induce hSARM1
302 activation. As expected, the control mutations E94R and K363A did not affect hSARM1 activity
303 either. Surprisingly, mutating the bulky W103, which stacks with the NAD+ nicotinamide ring, into
304 an alanine had only a small effect. Nevertheless, W103D mutation did have strong activating
305 effect, leading to the notion that NAD+ contacts with the W103 side chain may be dispensable for
306 the NAD+ inhibitory effect, but interference (as by the aspartate side chain) cannot be tolerated.
307 Interestingly, we did not find a density indicating the presence of an NAD+ molecule at the TIR
308 domain active site, although this site is not occluded by the ARM domain (Figure 5 - Figure

309 supplement 1B). Possibly, the BB loop, which is interacting with a neighboring ARM domain

310 (Figure 5 - Figure supplement 1B), assumes a conformation that prevents NAD+ entry into the

311 binding cleft.

312 Another conspicuous distinction between the two maps is the difference in local resolution of the

313 domains. The difference between the highest and lowest resolution domains (SAM>ARM>TIR) is

314 more obvious in the GraFix-ed structure than the NAD+ supplemented structure (Figure 2 -

315 Figure supplement 2). This implies that there is more flexibility in the GraFix-ed structure. A likely

316 reason for the difference in map homogeneity is that, while the compact arrangement in the

317 GraFix-ed structure is artificially imposed by high glycerol concentration, the NAD+ supplement

318 seems to induce a more natural compact folding.

319

320 **Discussion**

321 Our octamer ring structure of a near-intact hSARM1 reveals an inhibited conformation, in which

322 the catalytic TIR domains are kept apart from each other, unable to form close homodimers,

323 which are required for their NADase activity. This inhibited conformation readily disassembles

324 and gains most of its potential activity during protein purification, substantiating our hypothesis

325 that a low-affinity cellular factor inhibits hSARM1 is lost in purification. We have tested a few

326 candidate molecules and found that NAD+ induces a dramatic conformational shift in purified

327 hSARM1, from a disassembled outer ring to a compact two-ring structure, through binding to a

328 distal allosteric site from the TIR catalytic domain. Point mutations in this distal site promoted

329 hSARM1 activity in cultured cells and demonstrates their key allosteric role for inhibition of the

330 NADase activity. We also found that hSARM1 is inhibited *in vitro* by NAD+ for NADase activity,

331 demonstrating a 'substrate inhibition mechanism', as was also reported by another recent study

332 (Jiang et al., 2020).

333 Following these results, we propose a model for hSARM1 inhibition in homeostasis and activation

334 under stress (Figure 6). In this model, we suggest that hSARM1 is kept inhibited by NAD+

335 through its allosteric site, located at the ARM domain 'horns' junction that induces the compact

336 inhibited conformation. This state persists as long as NAD+ remains at normal cellular levels

337 [these are controversial, and range between 0.1mM (Cambronne et al., 2016) to 0.4-0.8mM

338 (Hara et al., 2019; Houtkooper et al., 2010; Liu et al., 2018b)]. However, upon a drop in the

339 cellular NAD+ concentration below a critical threshold, such as in response to stress, NAD+

340 dissociates from the allosteric inhibitory site. This triggers the disassembly of the compact

341 conformation, and the dimerization of TIR domains, which enables TIR's NADase activity and

342 NAD+ hydrolysis. The consequence is a rapid decrease in NAD+ cellular levels, leading to

343 energetic catastrophe and cell death.

344 This model seems to be at odds with another suggested mechanism (Bratkowski et al., 2020;

345 Zhao et al., 2019) in which, following axon injury, an increase in NMN concentration triggers

346 SARM1 activation. Regardless of the question whether axon injury actually leads to lasting NMN
347 levels elevation (Di Stefano et al., 2015) or not (Sasaki et al., 2016), we believe that the two
348 models can be easily reconciled, at least in the limited scope of the *in-vitro* enzymatic
349 mechanism. It is likely that NMN, a moiety of NAD+, will form interactions with most of the ARM[1]
350 residues as NAD+. By that, NMN will compete with NAD+ and prevent the formation of ARM[1]-
351 ARM[2] NAD+ bridge, the latter stabilizing the inactive conformation of SARM1. Such NAD+
352 displacement would result with SARM1 NADase activation. Clearly, this will require high NMN
353 concentrations to effectively compete-off the ARM[1]-ARM[2] bound NAD+. Indeed, we show (Figure
354 3E) that only 1mM NMN (but not 0.2mM) induce a moderate increase in SARM1 NADase activity
355 at 50 µM NAD+.
356 This finding casts some doubt over the prospects for activation by NMN to be naturally occurring
357 *in vivo*, as it consistently appears that NMN concentrations are not higher than 5 µM, and in any
358 case 10-200 times lower than that of NAD+ (Di Stefano et al., 2015; Liu et al., 2018b; Sasaki et
359 al., 2016). Therefore, while NMN could activate SARM1 *in-vitro*, in cultured cells engineered to
360 over produce NMN, or by exogenous supplement of NMN or NMN analogs, it is less likely to
361 occur *in-vivo*. Suggesting that the release of substrate inhibition due to the drop in NAD+ levels is
362 the key event in SARM1 activation.
363
364

Materials and methods

Key Resources Table				
Reagent type (species) or resource	**Designation**	**Source or reference**	**Identifiers**	**Additional information**
gene (homo sapiens)	SARM1	Imagene	uniprot Q6SZW1	
cell line (homo sapiens)	HEK293F	Thermo Fisher Scientific	Cat#R79007	
cell line (homo sapiens)	HEK293T	ATCC	CRL-11268	
transfected construct (mammalian vector)	pEGFP-N1	Clontech		modified
chemical compound, drug	Polyethyleneimine 40 kDa	Polysciences	PEI-MAX	
chemical compound, drug	Resazurin sodium salt	SIGMA	R7017	
chemical compound, drug	NAD+	SIGMA	NAD100-RO	
chemical compound, drug	FMN	SIGMA	F8399	
chemical compound, drug	ADH	SIGMA	A3263	
chemical compound, drug	Diaphorase	SIGMA	D5540	

chemical compound, drug	BSA	ORNAT	B9001S	
chemical compound, drug	eNAD	SIGMA	N2630	
software, algorithm	MotionCorr2	(Li et al., 2013)		
software, algorithm	Gctf	(Zhang, 2016)		
software, algorithm	Cryosparc V2	(Punjani et al., 2017)		
software, algorithm	SCIPION wrapper	(Martinez et al., 2020)		
software, algorithm	Warp	(Tegunov and Cramer, 2019)		
software, algorithm	CCP4	(Winn et al., 2011)		
software, algorithm	GESAMT	(Krissinel, 2012)		
software, algorithm	MOLREP	(Vagin and Teplyakov, 2010)		
software, algorithm	Coot	(Emsley et al., 2010)		
software, algorithm	REFMAC5	(Murshudov et al., 2011)		
software, algorithm	JLIGAND	(Lebedev et al., 2012)		

366

cDNA generation and subcloning.

Cloning of all the constructs was made by PCR amplification from the complete cDNA clone (Imagene) of hSARM1 (uniprot: Q6SZW1). For expression in mammalian cell culture, the near-intact hSARM1[w.t.] ([26]ERL…GPT[724]) and the mutants hSARM1[E642Q], hSARM1[RR216-7EE], hSARM[FP255-6RR], hSARM1[RR216-7EE/FP255-6RR] and delARM ([387]SAL…GPT[724]) constructs were ligated into a modified pEGFP-N1 mammalian expression plasmid which is missing the C-terminus GFP fusion protein, and includes N-terminal 6*HIS-Tag followed by a TEV digestion sequence. Assembly PCR mutagenesis (based on https://openwetware.org/wiki/Assembly_pcr) was used to introduce all the point mutations.

Protein expression and purification

For protein purification, SARM1[w.t.] and SARM1[E642Q] were expressed in HEK293F suspension cell culture, grown in FreeStyle[TM] 293 medium (GIBCO), at 37°C and in 8% CO_2. Transfection was carried out using preheated (70°C) 40 kDa polyethyleneimine (PEI-MAX) (Polysciences) at 1mg of plasmid DNA per 1 liter of culture once cell density has reached $1*10^6$ cells/ml. Cells were harvested 4- (in the case of SARM1[w.t.]) and 5- (in the case of SARM1[E642Q]) days after transfection by centrifugation (10 min, 1500 x g, 4°C), re-suspended with buffer A (50mM Phosphate buffer pH 8, 400mM NaCl ,5% glycerol, 1mM DTT, 0.5mM EDTA, protease inhibitor cocktail from Roche) and lysed using a microfluidizer followed by two cycles of centrifugation (12000 x g 20 min). Supernatant was then filtered with 45μm filter and loaded onto a pre-equilibrated Ni-chelate column. The column was washed with buffer A supplemented with 25mM Imidazole until a stable baseline was achieved. Elution was then carried out in one step of 175mM Imidazole, after which protein-containing fractions were pooled and loaded onto pre-equilibrated Superdex 200 HiLoad 16/60 (GE Healthcare) for size exclusion chromatography and elution was performed with 25mM Phosphate buffer pH 8.5, 120 mM NaCl, 2.5% glycerol, and 1mM DTT. In SDS-PAGE Coomassie staining, SARM1 appears as a doublet band (Figure 1B). This is probably a result of N-terminal His-tag truncation in some of the SARM1 protein molecules, due to our observation that only the upper band appears in anti-His WB. Protein-containing fractions were pooled and concentrated using a spin concentrator to 1.5 mg/ml. The concentrated proteins were either split into aliquots, flash-frozen in liquid N_2 and stored at -80°C for later cryo-EM visualization and enzymatic assays, or immediately subjected to a 'GraFix' (Kastner et al., 2008) procedure as follows. Ultracentrifugation was carried out using a SW41Ti rotor at 35,000rpm for 16 h at 4 °C in a 10– 30% glycerol gradient (prepared with gradient master-ip® BioComp Instruments, Fredericton, Canada), with a parallel 0–0.2% glutaraldehyde gradient, and with buffer composition of 25mM Phosphate buffer pH 8.5, 120mM NaCl, and 1mM DTT. The protein solution volume that was applied to GraFix was 0.4ml. After ultracentrifugation, the 12ml gradient tube content was carefully fractionated into 0.75ml fractions, supplemented with 10mM aspartate pH 8 to quench

404 crosslinking, using a regular pipette. Most of the cross-linked protein was found at the fractions

405 around 18% glycerol with minor amount at the bottom of the tube (See Figure 1B). Analysis was

406 made by SDS-PAGE and the dominant 2-3 fractions were pooled and diluted by 25mM

407 Phosphate buffer pH 8.5, 120mM NaCl, and 1mM DTT, so to reach a final glycerol concentration

408 of 2.5%. The diluted sample was then concentrated using a 100KDa cutoff Centricon® spin

409 concentrator to reach 1mg/ml protein concentration.

410

411 **Cryo-EM grids preparation**

412 Cryo-EM grids were prepared by applying 3 µl protein samples to glow-discharged (PELCO

413 easiGlow™ Ted Pella Inc., at 15 mA for 1 minute) holey carbon grids (Quantifoil R 1.2/1.3, Micro

414 Tools GmbH, Germany). The grids were blotted for 4 seconds and vitrified by rapidly plunging

415 into liquid ethane at −182 °C using Leica EM GP plunger (Leica Microsystems, Vienna, Austria).

416 The frozen grids were stored in liquid nitrogen until the day of cryo-EM data collection.

417

418 **Cryo-EM data acquisition and processing**

419 In this paper we present data that were collected with three separate cryo-electron microscopes:

420   1) F30 Polara in Ben-Gurion University, Israel was used for all sample preparation

421 optimization. It was also used to collect data sets without and with potential inhibitors (shown in

422 Figure 1C and the ATP and NMN supplemented classes in Figure 4B). Finally, it was used for

423 data collection and the 3D reconstructions presented in Figure 1D.

424 Samples were imaged under low-dose conditions on a FEI Tecnai F30 Polara microscope (FEI,

425 Eindhoven) operating at 300kV. Datasets were collected using SerialEM (Mastronarde, 2005) on

426 a K2 Summit direct electron detector fitted behind an energy filter (Gatan Quantum GIF) with a

427 calibrated pixel size of 1.1Å. The energy filter was set to remove electrons > ±10eV from the

428 zero-loss peak energy. The defocus range was set from -1.0µm to -2.5µm. The K2 summit

429 camera was operated in counting mode at a dose rate of 8 electrons/pixel/second on the camera.

430 Each movie was dose fractionated into 50 image frames, with total electron dose of $80ē/Å^2$.

431 Dose-fractionated image stacks were aligned using MotionCorr2 (Li et al., 2013), and their

432 defocus values estimated by Gctf (Zhang, 2016). The sum of the aligned frames was used for

433 further processing and the rest of the processing was done in Cryosparc V2 (Punjani et al.,

434 2017). Particles were auto-picked and subjected to local motion correction to correct for beam-

435 induced drift and then 2D classification with 50 classes. The best (based on shape, number of

436 particles and resolution) classes were manually selected containing 5459 (for hSARM1^{E642Q}) and

437 43868 (for SAM$^{1-2}$) particles. 1 initial 3D reference was prepared from all particles and 3D

438 refinement imposing C8 symmetry resulted the final map.

439   2) Titan Krios in ESRF CM01 beamline (Kandiah et al., 2019) at Grenoble, France, was
440 used for data collection and 3D reconstruction of the GraFix-ed (Figures 2 and 3) and NAD+
441 supplemented (Figure 5, Figure 5 - Figure supplement 1) samples.
442 Frozen grids were loaded into a 300kV Titan Krios (ThermoFisher) electron microscope (CM01
443 beamline at ESRF) equipped with a K2 Summit direct electron-counting camera and a GIF
444 Quantum energy filter (Gatan). Cryo-EM data were acquired with EPU software (FEI) at a
445 nominal magnification of ×165,000, with a pixel size of 0.827 Å. The grid of the GraFix-ed sample
446 was collected in two separate sessions. The movies were acquired for 7 s in counting mode at a
447 flux of 7.06 electrons per $Å^2\,s^{-1}$ (data collection 1: 3748 movies) or 6.83 electrons per $Å^2\,s^{-1}$ (data
448 collection 2: 4070 movies), giving a total exposure of ~50 electrons per $Å^2$ and fractioned into
449 40 frames. 7302 movies of the of the NAD+ supplemented grid sample were acquired for 4 s in
450 counting mode at a flux of 7.415 electrons per $Å^2\,s^{-1}$, giving a total exposure of ~40 electrons per
451 $Å^2$ and fractioned into 40 frames. For each data collection a defocus range from −0.8μm to
452 −2.8 μm were used. Using the SCIPION wrapper (Martinez et al., 2020) the imported movies
453 were drift-corrected using MotionCor2 and CTF parameters were estimated using Gctf for real-
454 time evaluation. Further data processing was conducted using the cryoSPARC suite. Movies
455 were motion-corrected and contrast transfer functions were fitted. Templates for auto-picking
456 were generated by 2D classification of auto picked particles. For the GraFix-ed data, template-
457 based auto-picking produced a total of 658,575 particles, from which 147,232 were selected
458 based on iterative reference-free 2D classifications for reconstruction of the GraFix-ed structure.
459 In the case of the NAD+ supplemented data, a total of 335,526 particles were initially picked, from
460 which 159,340 were selected based on iterative reference-free 2D classifications for
461 reconstruction. Initial maps of both GraFix-ed and NAD+ supplemented hSARM1 were calculated
462 using Ab-initio reconstruction and high-resolution maps were obtained by imposing C8-symmetry
463 in non-uniform 3D refinement. Working maps were locally filtered based on local resolution
464 estimates.
465   3) Talos Glacios in EMBL, Grenoble, France was used for data collection and the
466 comparison of NAD+ supplemented and not-supplemented samples (Figure 4A,B).
467 Frozen grids were loaded into a 200kV Talos Glacios (ThermoFisher) electron microscope
468 equipped with a Falcon3 direct electron-counting camera (ThermoFisher). Cryo-EM data were
469 acquired with EPU software (FEI) at a nominal magnification of ×120,000, with a pixel size of
470 1.224Å. For the comparative analysis of NAD+ supplement, the grids of +5mM NAD and no NAD
471 sample were screened and collected. The movies were acquired for 1.99 s in linear mode at a
472 flux of 21.85 electrons per $Å^2\,s^{-1}$ (data collection +5mM NAD: 2408 movies; no NAD: 2439
473 movies) giving a total exposure of ~44 electrons per $Å^2$ and fractioned into 40 frames. For each
474 data collection a defocus range from −0.8μm to −2.8μm was used. Warp (Tegunov and Cramer,
475 2019) was used for real-time evaluation, for global and local motion correction and estimation of

476 the local defocus. The deep learning model within Warp detected particles sufficiently. Inverted

477 and normalized particles were extracted with a boxsize of 320 pixels.

478 466135 particles of the +5 mM NAD data, and 414633 particles of the 'no NAD+' set were

479 imported into Cryosparc for further processing and subjected to a 2D circular masked

480 classification with 100 classes. The class averages were manually evaluated and designated as

481 either 'full ring' or 'core ring'.

482

483 **Cell viability assay**

484 HEK293T cells were seeded onto lysine precoated 24 well plates (100,000 cells in

485 each well) in final volume of 500 µL of DMEM (10% FBS) and incubated overnight at 37°C under

486 5% CO_2. They were then transfected with different hSARM1 constructs using the calcium

487 phosphate-mediated transfection protocol (Kingston et al., 2003), with addition of 25µM

488 Chloroquine (SIGMA) right before the transfection. 6 hours after transfection, the chloroquine-

489 containing DMEM was replaced by fresh complete medium. After 24 hours the medium was

490 removed and replaced with 0.03 mg/ml Resazurin sodium salt (SIGMA) dissolved in Phenol Red

491 free DMEM. All plates were then incubated for 1h at 37°C and measured using a SynergyHI

492 (BioTek) plate reader at 560nm excitation and 590nm emission wavelengths. All fluorescent

493 emission readings were averaged and normalized by subtracting the Resazurin background

494 (measured in wells without cells) and then divided by the mean fluorescence emission from cells

495 transfected by the empty vector (pCDNA3).

496 HEK293F cells were seeded in 24 well plates (1 million cells in each well) in a final

497 volume of 1 mL of FreeStyle™ 293 medium (GIBCO). The cells were transfected with 1 ug DNA

498 as described before and incubated at 37°C and in 8% CO_2. Live cells were counted using the

499 trypan blue viability assay every 24 hours for three days. Three repeats were performed for each

500 construct.

501 Noteworthy, the identity of the HEK293F and HEK293T cell lines is clear by their

502 different growth conditions and features.

503

504 *in vitro* **hSARM1 NADase activity assays**

505 For quantitation of hSARM1 NADase activity and the inhibitory effect of selected

506 compounds (Figure 3F; Figure 4A and D), purified hSARM1[w.t.] and hSARM1[E642Q] proteins were

507 first diluted to 400 nM concentration in 25 mM HEPES pH 7.5, 150mM NaCl, and then mixed in

508 25°C with 1uM of NAD+ (in the same buffer) with a 1:1 v/v ratio. All inhibitors were diluted with

509 the same buffer, and the pH values were measured and if necessary titrated to 7.5. Inhibitors

510 were pre-incubated for 20 min with hSARM1 in 25°C before mixing with NAD+. At designated

511 time points, reactions were quenched by placing the reaction tubes in 95°C for 2 min.

512 Measurement of NAD+ concentrations was made by a modified enzymatic coupled cycling assay
513 (Kanamori et al., 2018). The reaction mix, which includes 100 mM Phosphate buffer pH=8, 0.78%
514 ethanol, 4uM FMN (Riboflavin 5'-monophosphate sodium salt hydrate), 27.2 U/ml Alcohol
515 dehydrogenase (SIGMA), 1.8 U/ml Diaphorase (SIGMA) and freshly dissolved (in DDW) 8 uM
516 Resasurin (SIGMA), was added to each sample at 1:1 (v/v) ratio and then transferred to a 384-
517 well black plate (Corning). Fluorescent data were measured using a SynergyHI (BioTek) plate
518 reader at 554-nm excitation and 593-nm emission wavelengths. Standard curve equation for
519 calculation of NAD+ concentration was created for each assay from constant NAD+
520 concentrations.

521   eNAD-based NADase assay: eNAD (Nicotinamide 1,N[6]-ethenoadenine dinucleotide,
522 SIGMA – N2630) was solubilized in water and mixed with native NAD+ in ration of 1:10 (mol:mol)
523 to a final stock concentration of 10mM. Serial dilutions were made with 25mM HEPES pH 7.5,
524 150mM NaCl buffer and the final mix was transferred to a 384-well black plate (Corning).
525 Reaction started by the addition of hSARM1 to a final concentration 400nM. Then, eNAD
526 degradation rate was monitored by fluorescence reading (330-nm excitation and 405-nm
527 emission wavelengths) of the plate using a SynergyHI (BioTek) in 25°C for 3 hours. For each
528 NAD+ concentration, a control reaction without SARM1 was measured and subtracted from the
529 +hSARM1 reading and the slope of the linear area was calculated. For the final plot, average of
530 slopes from 3 separate assays for each concentration was calculated.

531   HPLC analysis: Purified hSARM1[w.t.] was first diluted to 800nM in 25mM HEPES pH
532 7.5, 150mM NaCl, and then mixed at 37°C with different concentrations of NAD+ (in the same
533 buffer) in a 1:1 v/v ratio and incubated for 0, 5 and 30 min. 1:100 (v/v). BSA (NEB Inc. 20mg/ml)
534 was included, and reactions were stopped by heating at 95°C for 2 minutes. Where specified,
535 NMN (Sigma-Aldrich - N3501) was added in different concentrations. For control, NAD+
536 consumption was compared to a commercially available porcine brain NADase 0.025 units/ml
537 (Sigma-Aldrich - N9879). HPLC measurements were performed using a Merck Hitachi Elite
538 LaChrom HPLC system equipped with an autosampler, UV detector and quaternary pump. HPLC
539 traces were monitored at 260nm and integrated using EZChrom Elite software. 10 µL of each
540 sample were injected onto a Waters Spherisorb ODS1 C18 RP HPLC Column (5 µm particle size,
541 4.6 mm × 150 mm ID). HPLC solvents are; A: 100% methanol; B: 120mM sodium phosphate pH
542 6.0; C double-distilled water (DDW). The column was pre-equilibrated with B:C mixture ratio of
543 80:20. Chromatography was performed at room temperature with a flow rate of 1.5 ml/min. Each
544 analysis cycle was 12 min long as follows (A:B:C, v/v): fixed 0:80:20 0-4 min; gradient to 20:80:0
545 4-6 min; fixed 20:80:0 from 6-9 min, gradient to 0:80:20 from 9-10 min; fixed 0:80:20 from 10-12
546 min. The NAD+ hydrolysis product ADPR was eluted at the isocratic stage of the chromatography
547 while NAD+ elutes in the methanol gradient stage.

548

Calculation of SARM1 kinetic parameters

For V_{max} and K_m determination, the NADase activity assay was performed with several different NAD+ substrate concentrations and sampled in constant time points. For each NAD+ concentration, linear increase zone was taken for slope (V_0) calculation. All data were then fitted to the Michaelis-Menten equation using non-linear curve fit in GraphPad Prism software. K_{cat} was calculated by dividing the V_{max} with protein molar concentration.

Model building and refinement

GraFix-ed map

The monomers of known octameric X-ray structures of the hSARM1 SAM[1-2] domains (PDBs 6qwv and 6o0s) were superimposed by the CCP4 (Winn et al., 2011) program GESAMT (Krissinel, 2012) to identify the conserved regions. The model chosen for MR (molecular replacement) contained single polypeptide residues A406-A546 from the PDB 6qwv (SAM Model). Superposition of all available structures of the hSARM1 TIR domain (PDBs 6o0q, 6o0r, 6o0u, 6o0qv, and 6o1b) indicated different conformations of the protein main chain for the BB loop region (a.a 593-607). Two different MR models were prepared for the hSARM1 TIR domain. TIR Model 1 contained regions 562-592 and 608-700 of the high-resolution structure (PDB 6o1b). TIR Model 2 represented assembly of superimposed polyalanine models of all the available hSARM1 TIR domains. Models were positioned into the density map by MR with use of phase information as implemented in program MOLREP (Vagin and Teplyakov, 2010). The shell scripts of the MOLREP EM tutorial were downloaded from https://www.ccpem.ac.uk/docs.php and adapted to allow simultaneous positioning of eight molecular symmetry related SARM1 copies (MOLREP keyword NCS 800).

The search protocol involved Spherically Averaged Phased Translation Function (SAPTF; MOLREP keyword PRF Y). The recent version of MOLREP (11.7.02; 29.05.2019) uses modification of the original SAPTF protocol (Vagin and Isupov, 2001), adapted for work with EM density maps (Alexey Vagin, private communication). It now performs the Phased RF (rotation function) search step in a bounding box of the search model and not in the whole (pseudo) unit cell. Instead of Phased Translation Function step, MOLREP performs Phased RF search at several points in the vicinity of SAPTF peak and, in addition, applies Packing Function to potential solutions.

The SAM Model was positioned into the GraFix-ed density map with a score (Map CC times Packing Function) of 0.753. The positioned SAM Model was used as a fixed model in MOLREP when searching for the TIR domain. The TIR Model 1 was positioned with a score of 0.582. The MR search with the TIR Model 2 gave essentially the same solution with a lower overall score of 0.559, but higher contrast. With both SAM[1-2] and TIR domains positions fixed, the MR search for an ideal 10-residue α-helical model allowed location of 64 fragments (8 helices per SARM1

586 monomer) with scores in the range of 0.78-0.81. These helical fragments were used for building
587 of the ARM domain in Coot (Emsley et al., 2010). The quality of the high resolution GraFix-ed
588 density map was sufficient for assignment of side chains for all ARM domain residues. The TIR
589 domain BB loop region (a.a 595-607) was built to fit a relatively poor density map in a
590 conformation different to those observed in X-ray structures. The model was refined using
591 REFMAC5 (Murshudov et al., 2011). Side chains of some Lys residues had blobs of undescribed
592 density attached to them. These were modelled as glutaraldehyde ligands. Geometrical restraints
593 for the di-glutaraldehyde molecule and its links to side chains of Lys residues were prepared
594 using JLIGAND (Lebedev et al., 2012). The dictionary file was manually edited to allow links to
595 more than a single lysine residue.
596
597 *NAD-supplemented map*
598 Originally, the refined full-length GraFix-ed model was positioned by MR into the NAD-
599 supplemented density map, but differences in the relative positions of the hSARM1 domains were
600 apparent. Therefore, MR search was conducted for separate hSARM1 domains. The SAM Model
601 was positioned with a score of 0.653 into this map. With the fixed SAM Model the TIR Model 1
602 was found with score of 0.594. With fixed SAM and TIR Models, the ARM domain from the
603 GraFix model was found with score of 0.623. The BB-loop of the TIR domain was built into well-
604 defined density map in a conformation not observed in any of the X-ray structures and different to
605 that in the GraFix-ed model. A low sigma cutoff map allowed modelling of the loop connecting the
606 SAM and TIR domains. Inspection of the maps indicated NAD+ binding accompanied by
607 structural re-arrangement of the ARM[1]-ARM[2] linker region (a.a. 312-324).
608
609 **Accession numbers**
610 Coordinates and structure factors have been deposited in the Protein Data Bank with
611 accession numbers 6ZFX, 7ANW, 6ZG0, 6ZG1, and in the EMDB with accession numbers
612 11187, 11834, 11190, 11191 for the GraFix-ed, NAD+ supplemented, not treated, and SAM[1-2]
613 models and maps, respectively.
614
615

Figure 1
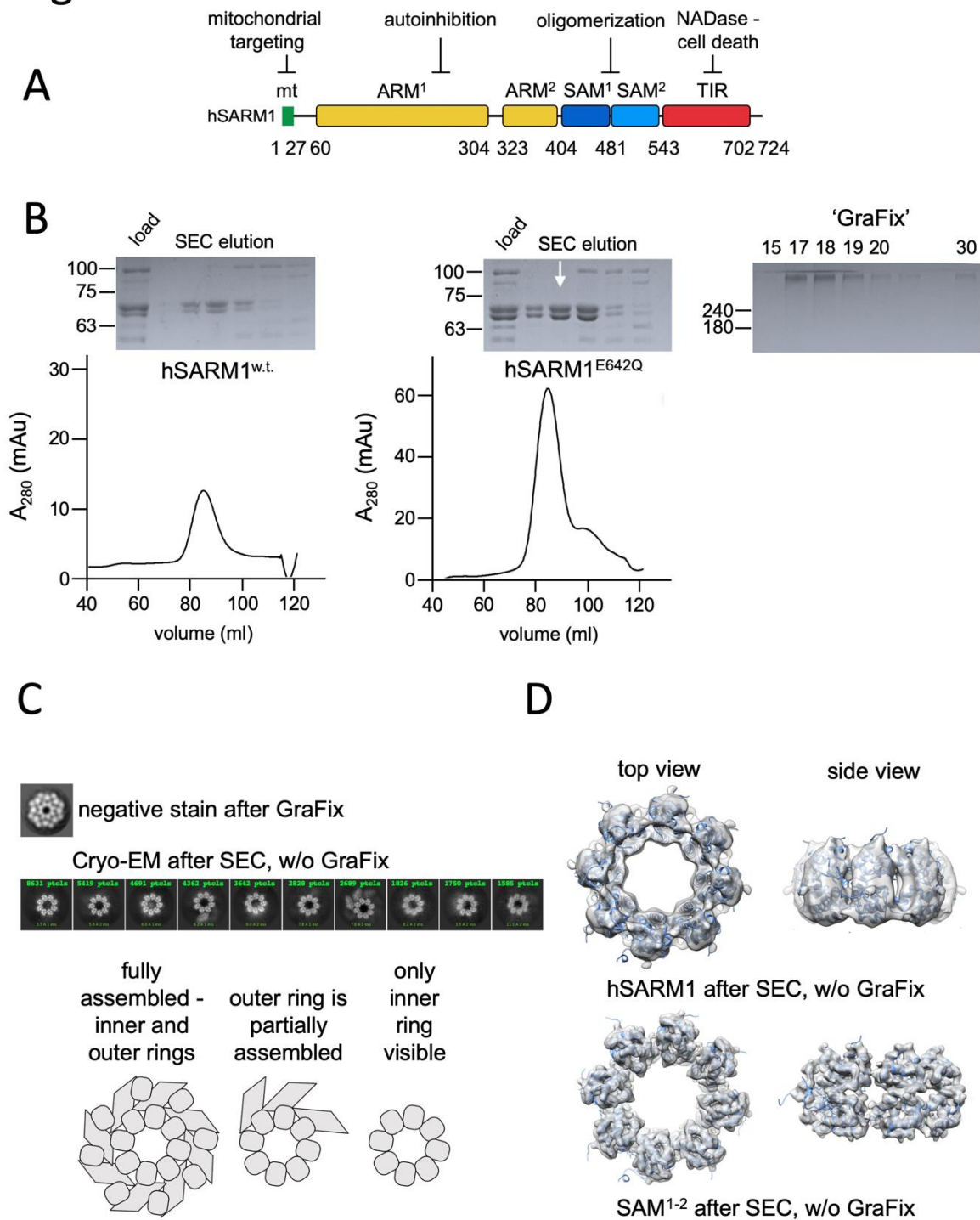
Figure 1. Domain organization and cryo-EM analysis of purified hSARM1.

A) Color-coded organization and nomenclature of the SARM1 ARM, SAM, and TIR domains. The position of mitochondrial localization signal is presented at the N terminus of the protein. Two constructs are used in this study, both missing the mitochondrial N-terminal sequence. hSARM1[E642Q] is a NADase attenuated mutant that was used in all the structural and some of the

622 biochemical experiments; while hSARM1[w.t.] was used in the NADase and cellular experiments. B)

623 hSARM1 protein preparations. Presented are SDS-PAGE analyses of size-exclusion

624 chromatography fractions after the initial metal-chelate chromatography step. Note the higher

625 yield of hSARM1[E642Q] compared to hSARM1[w.t.], and the doublet SARM1 bands, the result of a

626 partial N-terminal his-tag digestion. The white arrow indicates the fraction used for the

627 subsequent GraFix step shown at the right panel, where the approximate glycerol concentrations

628 of each fraction are indicated. C) Most-prevalent 2D class averages of hSARM1[E642Q] protein

629 preparations. A dramatic difference can be seen between the previously-conducted negative

630 stain analysis (top panel, as in (Sporny et al., 2019)) and typical cryo-EM (middle panel). While

631 the negative stain average clearly shows inner and peripheral rings (see illustration in the bottom

632 panel), most cryo-EM classes depict only the inner ring, and some a partial outer ring assembly.

633 Note that a gradient fixation (GraFix) protocol was applied before the negative stain but not the

634 cryo-EM measurements. D) 3D cryo-EM reconstructions of hSARM1[E642Q] (top panel) and SAM[1-2]

635 (bottom panel) and docking of the SAM[1-2] crystal structure (PDB code 6QWV) into the density

636 maps, further demonstrating that only the inner, SAM[1-2] ring is well-ordered in cryo-EM of purified

637 hSARM1[E642Q].

638

639

Figure 1—Figure supplement 1

```
                ARM¹        α1                    α2                 α3           α4              α5
                wwwwwwwww            wwwwwwwwwwwwwww        wwwwwwwww  wwwwwwwwwww      wwwwwwwwwww
               60          80              100           120              140
human      EVQDALERALPELQQALSALKQAG---GARAVGAGLAEVFQLVEEAWLLPAVGREVAQGLCDAIRLDGGLDLLLRLLQAP----ELETRVQAARLLEQIL
mouse      EVQGALERSLPELQQALSELKQAS---AARAVGAGLAEVFQLVEEAWLLPAVGREVAQGLCDAIRLDGGLDLLLRLLQAP----ELETRVQAARLLEQIL
zebrafish  DVQAVLDGSLPALRSAIRTLRSSKDTGDLEETRRAIAETFQLVEEAWLPTVGRRVAEEICNRIRLDGGLELLLQLMQTP----AVEITYESAKLLEQIL
C.elegans  AMMHTLKTKLSKYQAMMDKAFEEIAKVEDANIIEGCTIVRKLMRKVWNTPKVSADLANALCDYLRDRDYFDKLIKMFISPNTAACDQVRMECGKVLEECT
               :  .*.  *.  .:.             .  :  *.  .*:  ..:.* * *.  :*: :*: :*  . :: *:::: :*       : :..::**:

               α6         α7              α8           α9           α10              α11           α12
               wwwwwww  wwwwwwwww     wwwwwwwwwwww   wwwwwww    wwwwwwww      wwwwwwwwwww     wwwwwwww
               160            180            200                220          240
human      VAENRDRVARIGLG--VILNLAKEREPVELARSVAGILEHMFKHSEETCQRLVAAGGLDAVLYWCRRT--DPALLRHCALALGNCALHGGQAVQRRMVEK
mouse      VAENRDRVARIGLG--VILNLAKEREPVELARSVAGILEHMFKHSEETCQRLVAAGGLDAVLYWCRRT--DPALLRHCALALANCALHGGQTVQRCMVEK
zebrafish  VSENRDYVARMGLG--VILNLTREQEDAQLARSVSGILEHMFKHTEETSAQLITNGALDTILYWCRGT--DPTVLRHCAVALSNCAMYGGHRCQRLMIEK
C.elegans  SSANLEYIVNKSYTKKIMIVAMKLNKTPDQQRLSLSLIGNLFKHSNAVSLSLIETDVIDHIILTFKRAPECPDILRHAALALANILLYTCFEGKKKIIQK
               : *  *  :..      :::     : .: :  *    .:  :::***::  ..  *:  . :*  ::    : :    * :***.*:**.*  ::  ::  :::**

                   α13        α14        α15       α16   ARM¹                          ARM²  α1           α2
               wwwwwwwww   wwwwwwwwwwww   wwwwww   wwwwww  wwwwwwwwwww             wwwwwww        wwwwwww
               W    260         280W           300                320              340
human      RAAEWLFPLAFSKEDELLRLHACLAVAVLATNKEVEREVERSGTLALVEPLVASLDPGRFARCLVDASDTSQGRGPDDLQRLVPLLD-SNRLEAQCIGAF
mouse      RAAEWLFPLAFSKEDELLRLHACLAVAVLATNKEVEREVEHSGTLALVEPLVASLDPGRFARCLVDASDTSQGRGPDDLQSLVLLLD-SSRLEAQCIGAF
zebrafish  QAAEWLFPLAFSKEDELIRFHACLAVAVLAANREMEKEVVKSGTLELVEPFIASLDPDEFARNMLDSADSMQGRTAADLQHLLPLLD-GTRLEGKCIAAF
C.elegans  KIPEWLFFLAS-QADDVTRYYACIAVCTIVSVKEFEPLVRKSDTMKLVEPFLQVHDPATFAR---DYHKYAQGNTKEWLERLLPMLQPSRRREARSVAAF
               : .****  **   :  *:: : :**:  :  :.  :*.*   ::  :*.*  ::  **  ***    :**  ***   .  **.    *: *: :*:. . * *.::.**

                      α           α     α                    α      ARM²      SAM¹αN      α1      α2            α3
               wwwwwwwwww    wwww   wwwwwwwww      wwwwwwwwwww             www   wwwwwwww   www        wwwww
               360           V    380           400              420              440
human      YLCAEAAIKSLQGKTKVFSDIGAIQSLKRLVSYSTNGTKSALAKRALRLLGEEVPRRILPSVPSWKEAEVQTWLQQIGFSKYCESFREQQVDGDLLLRLT
mouse      YLCAEAAIKSLQGKTKVFSDIGAIQSLKRLVSYSTSALAKRALRLLGEEVPRRILPCVASWKEAEVQTWLQQIGFSQYCENFREQQVDGDLLLRLT
zebrafish  YLCVETSIKSRQRNTKIFQEIGAVQSLKRIVMYSSNATVCSLAKRALKMMSEEVPRRILSSVPNWKSGEVQTWLQQIGFSAFSERFQELQVDGDLLLNIT
C.elegans  HFTLEATIKKEQNKLDVFQEIGAIQALKEVAS-SPDEVAAKFASEALTVIGEEVPYKLAQQVPGWTCADVQYWVKKIGFEEYVEKFAKQMVDGDLLLQLT
               ::  *::**.  *  :  :*.:***:*:**.:.    .:  .  .  :*.**  ::*****  :    *..*  .:** *:::***.  :  *  *  :  ***:****.:*

               α4               α5    SAM¹     SAM²   α1          α2           α3      α4        α5
               wwww          wwwwwwwwwww             wwwww     wwwwwwwww    wwwww   wwwww    wwwww
               460              480          500              520          540
human      EEELQTDLGMKSGITRKRFFRELTELKTFANYSTCDRSNLADWLGSLDPRFRQYTYGLVSCGLDRSLLHRVSEQQLLEDCGIHLGVHRARILTAAREMLH
mouse      DEELQTDLGMKSSITRKRFFRELTELKTFASYSTCDRSNLADWLGSLDPRFRQYTYGLVSCGLDRSLLHRVSEQQLLEDCGIRLGVHRTRILSAAREMLH
zebrafish  EQDLIQDLGMTSGLTRKRFLRDLRVLKTYANYSTCDPNNLADWLADADPRFRQYTYGLVQSGVDRNNIVHITDQQLLTDCHVENGIHRAKILSAARRPSK
C.elegans  ENDLKHDVGMISGLHRKRFLRELQTLKVAADYSSVDESNLDNFLMGLSPELSVYTYQMLTNGVNRSLLSSLTDEMMQNACGITNPIHRLKLTQAFETAKH
               ::::*  *:**  *.:  ****:*:*  **.  *.:*::.   . **  ::*  . *:.:    ***  :::    *  *::*:***:..:**: *  *    :*******:  *:

               SAM²    TIR   βA          αA        βB    BB-loop      αB     βC     αC         αC'
                   w       wwwwwwwwwwwwww      wwwwwwwwwwwww        wwwww       www    wwwwwwwwwww
               560         580           600              620          640
human      SPLPCTGGKPSGDTPDVFISYRNSGSQLASLLKVHLQLHGFSVFIDVEKLEAGKFEDKLIQSVMGARNFVLVLSPGALDKCMQDHDCKDWVHKEIVTAL
mouse      SPLPCTGGKLSGDTPDVFISYRRNSGSQLASLLKVHLQLHGFSVFIDVEKLEAGKFEDKLIQSVIAARNFVLVLSAGALDKCMQDHDCKDWVHKEIVTAL
zebrafish  PCLTDSQPK----GPDVFISYRRTTGSQLASLLKVHLQLRGFSVFIDVEKLRGFEEKLITSVQRARNFILVLSANALDKCMGDVAMKDWVHKEIVTAL
C.elegans  P--DDVEVAMLSKQIDVFISYRRSTGNQLASLIKVLLQLRGYRVFIDVDVDKLYAGKFDSSLLKNIQAAKHFILVLTPNSLDRLLNDDNCEDWVHKELKCAF
                   . ********.:*.*****:** ***:*:  *****:**  *:*:...*:  .:  *::*:***:..:**:  *    :*******: *:

                  βD               αD    βE        αE                TIR
               ww         wwwwwwww              www     wwwwwwwww
               660           680          700              720
human      SCGKNIVPIIDG-FEWPEPQ-VLPEDMQAVLTFNGIKWSHEYQEATIEKIIRFLQGRSSRDSSAGSDTSLEGAAPMGPT-
mouse      SCGKNIVPIIDG-FEWPEPQ-ALPEDMQAVLTFNGIKWSHEYQEATIEKIIRFLQGRPSQDSSAGSDTSLEGATPMGLP-
zebrafish  NGKKNIVPVTDN-FVWPDPT-SLPEDMSTILKFNGIKWSHEYQEATIEKILRFLEGCPSQEKPDGAKTDKKEPQKK----
C.elegans  EHQKNIIPIFDTAFEFPTKEDQIPNDIRMITKYNGVKWVHDYQDACMAKVVRFITGELNRTTPTTKEMPSISRKTTQQRW
                   . ***:*:  *   *  :*         :*:*:  :  .:**:**  *:**:*  :  *::**:  *      :*******:  *:
```

```
human|Q6SZW1
mouse|Q6PDS3
zebrafish|F1QWA8
C.elegans|NP_497784.1
```

primary ARM-TIR docking site
secondary ARM-TIR docking site
ARM-ARM interaction site
ARM-SAM same-chain interaction site
ARM-SAM next-chain interaction site

641

642 Figure 1 - Figure supplement 1. Structure-based sequence alignment of the SARM1 of human,

643 mouse, zebrafish and the C. elegans homolog TIR-1. Color coded highlights and Uniprot protein

644 accession numbers are listed below.

hSARM1 construct and pre-treatment	hSARM1 GraFix-ed	hSARM1 +5mM NAD+	hSARM1 no treatment	SAM[1-2]
electron microscope	Titan Krios	Titan Krios	F30 Polara	F30 Polara
Cryo-EM acquisition and processing				
EMDB accession #	11187	11834	11190	11191
Magnification	165,000x	165,000x	200,000	200,000
Voltage (kV)	300	300	300	300
Total electron exposure (e^- / Å^2)	50	40	80	80
Defocus range (µM)	-0.8 to -2.8	-0.8 to -2.8	-1.0 to -2.5	-1.0 to -2.5
Pixel size (Å)	0.827	0.827	1.1	1.1
Symmetry imposed	C8	C8	C8	C8
Initial particles	658,575	335,526	26,496	416,980
Final particles	147,232	159,340	5,410	43,868
Resolution (masked FSC = 0.143, Å)	2.88	2.7	7.7	3.77
Model Refinement				
PDB ID	6ZFX	7ANW	6ZG0	6ZG1
Model resolution (FSC = 0.50/0.143Å)	3.6 / 2.9	2.9 / 2.7		
Model refinement resolution	2.88	2.70		
Non-hydrogen atoms	39,856	40,560		
Residues	5,080	5,176		
RMS deviations				
Bond length (Å)	0.008	0.009		
Bond angle (°)	1.84	1.84		
Ramachandran plot				
Favored (%)	89.05	91.68		
Allowed (%)	10.95	8.32		
Disallowed (%)	0	0		
Rotamer Outliers (%)	5.73	6.64		
Validation				
MolProbity score	2.68	2.49		
Clashscore	10.08	6.66		

645
646 Table 1: Cryo-EM data acquisition, reconstruction and model refinement statistics.
647
648
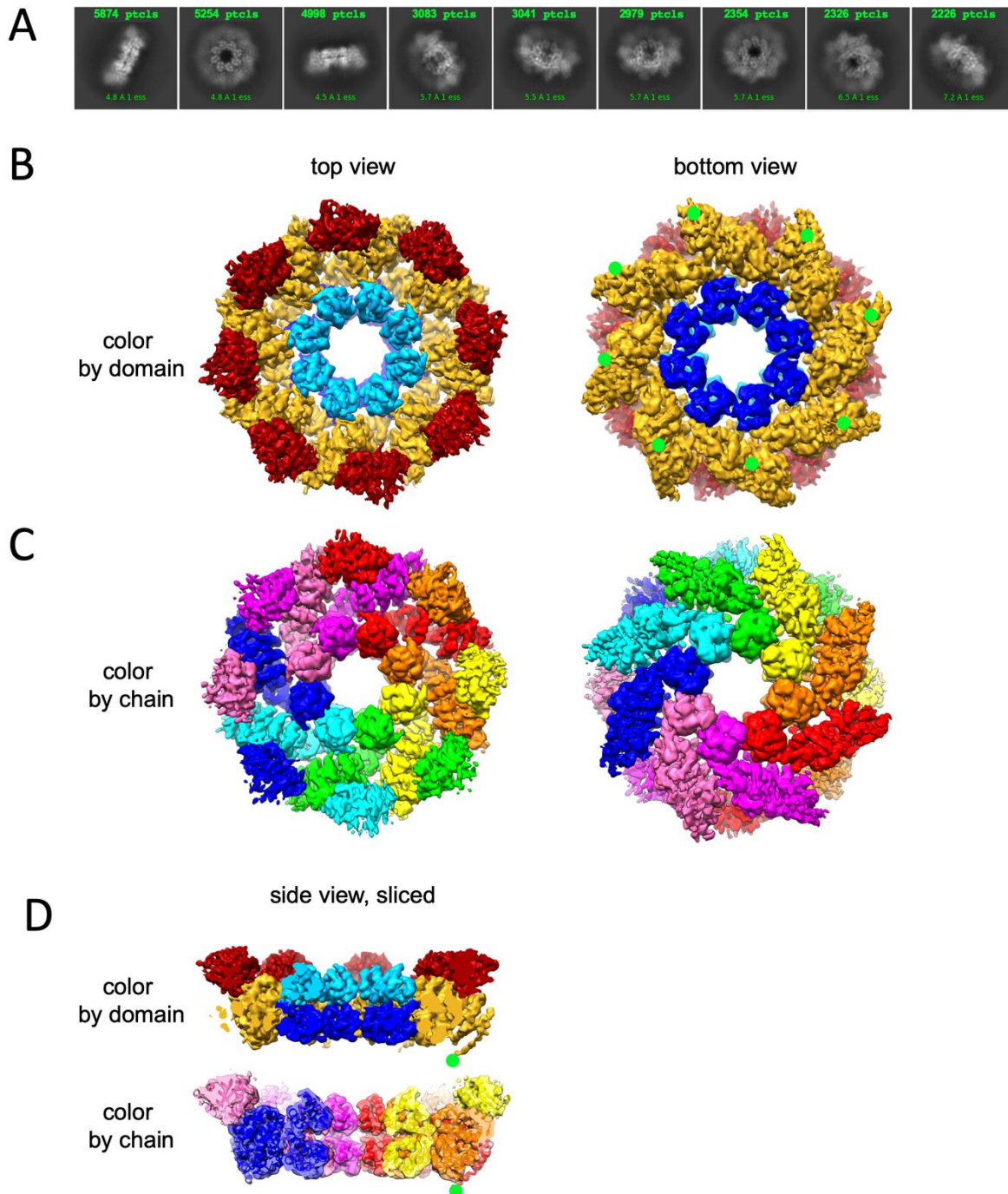
Figure 2

Figure 2. Cryo-EM structure of GraFix-ed hSARM1[E642Q].

A) Selected representation of 2D class averages used for the 3D reconstruction. The number of particles that were included in each average are indicated at the top of each class. B-D) Cryo-EM density map color-coded as in (Figure 1A) and by chain. 'Top view' refers to the aspect of the molecule showing the TIR (red) and SAM[2] (cyan) domains closest to the viewer, while in the

655 'bottom view' the SAM[1] (blue) domains and the illustrated mitochondrial N-terminal localization

656 tag (green dot - was not included in the expression construct) are the closest. D) Side view

657 representation of the structure, sliced at the frontal plane of the aspect presented in (B) and (C).

658

659

Figure 2 - Figure supplement 1

A

top view

bottom view

203 Å

side view

80 Å

B

180°

ARM
"crescent horns"
region

660
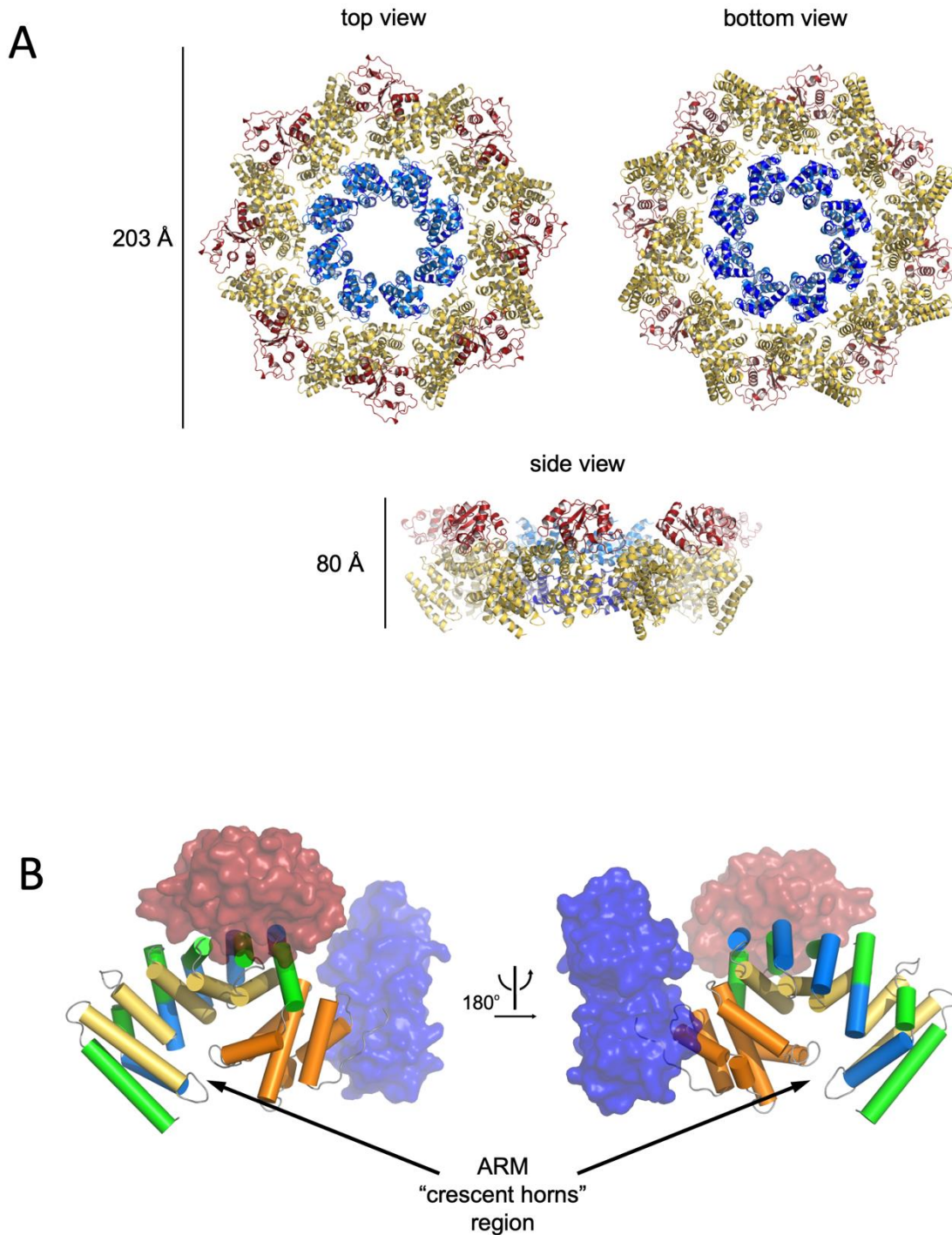
Figure 2 - Figure supplement 1. A) Cartoon model of hSARM1. Color code is as in Fig. 1A. B)
Architecture of the crescent-shaped ARM domain. The structure reveals that there are two ARM
subdomains, one spanning res. 60-303 with five 3-helix (depicted as green, yellow and blue
cylinders) ARM repeats, and the second (res. 322-400) with two repeats, all colored in orange.
The SAM and TIR domains are represented as transparent blue and red surface, respectively.

666
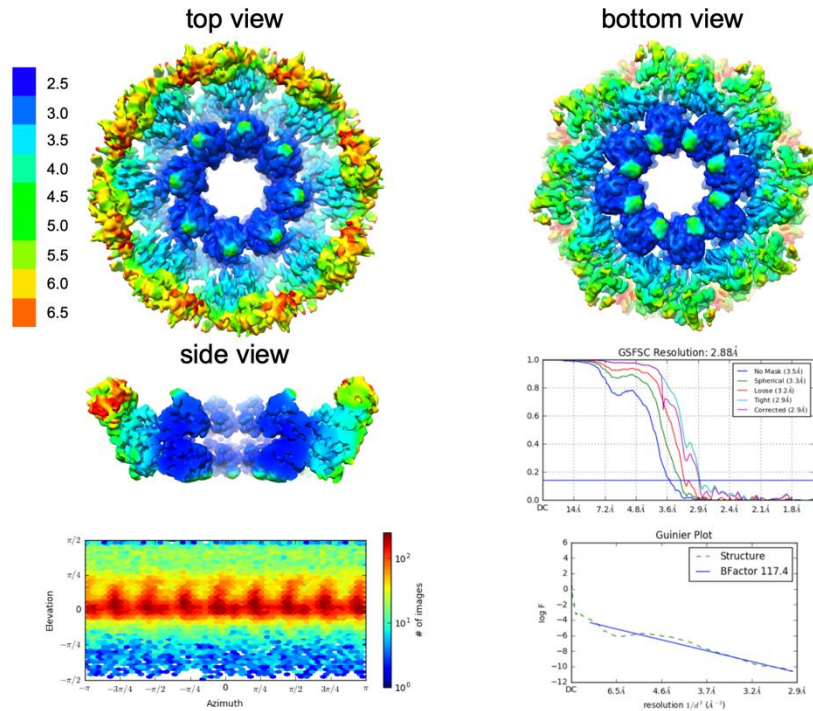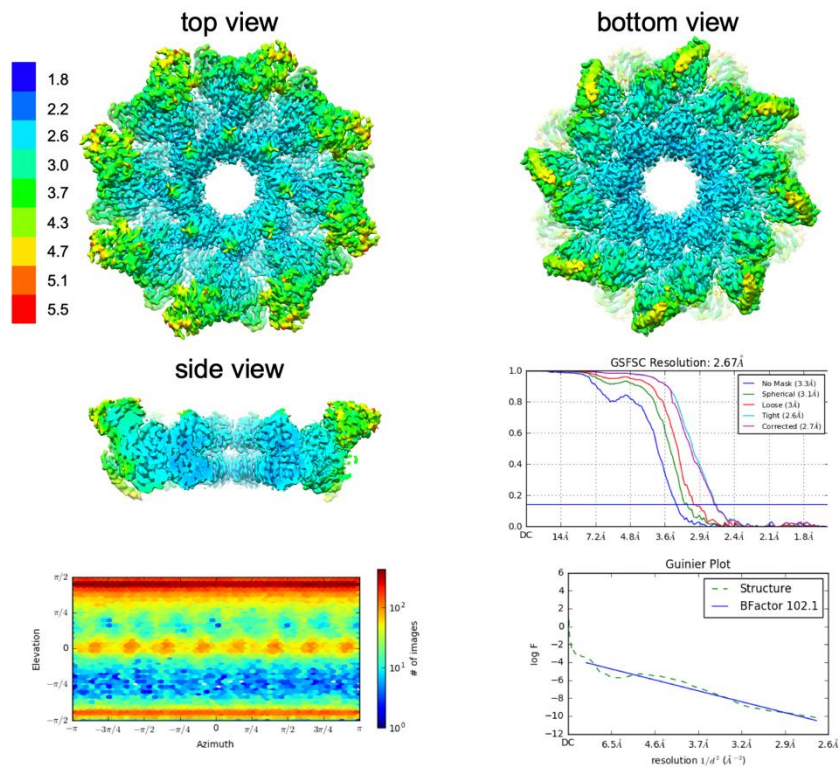
Figure 2 - Figure supplement 2. Resolution, angular distribution, and B-factor estimations of the
Cryo-EM maps of GraFix-ed (upper panel) and NAD+ supplemented (bottom panel) hSARM1.
Note that while the GraFix-ed map has an overall lower resolution, it has a heterogenous
distribution with distinctive differences between the SAM, ARM and TIR regions. On the contrary,
in the NAD+ supplemented map, resolution values are much more homogenous.

672
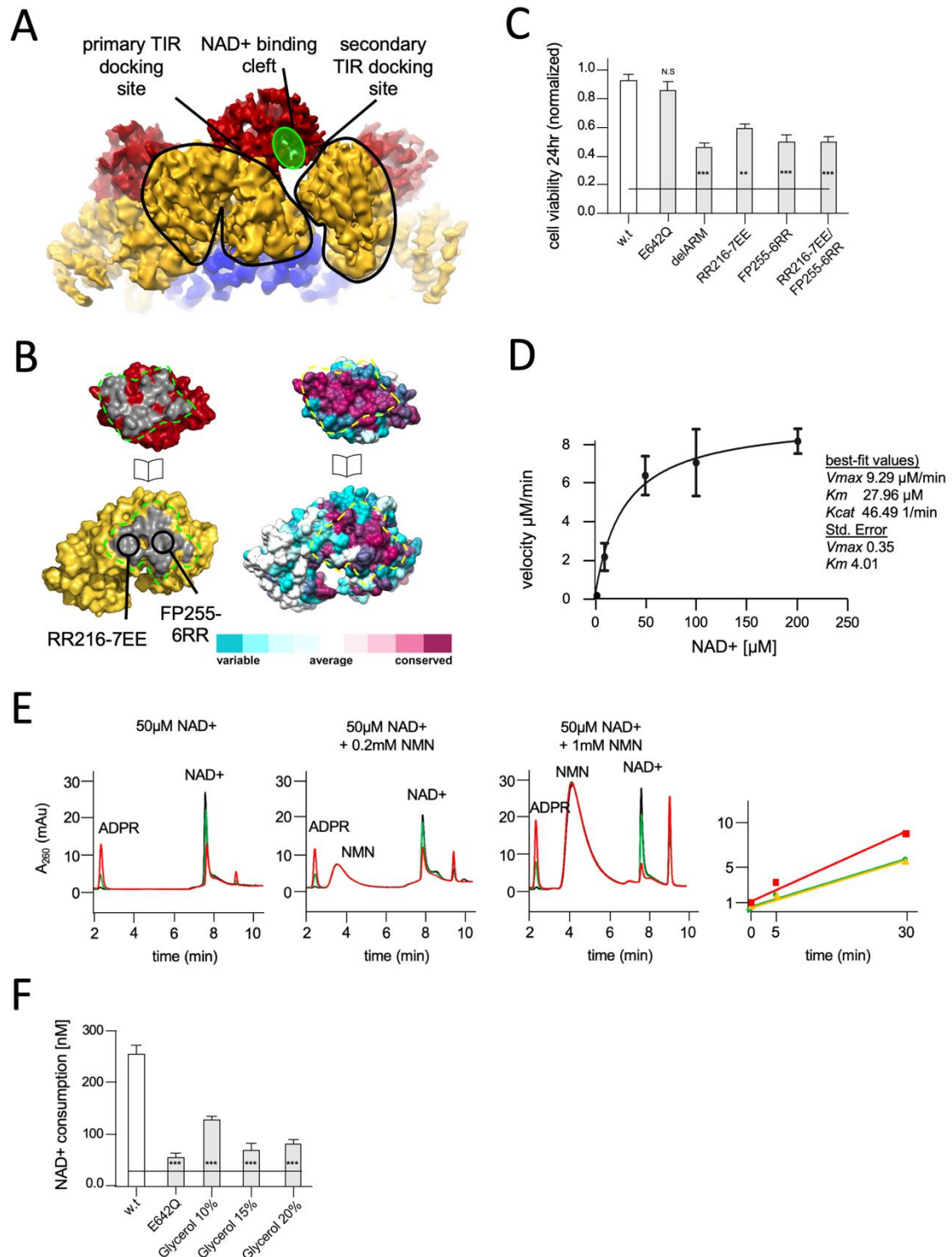
Figure 3. Structural basis for hSARM1 auto-inhibition.

A) Close-up of a tilted side view of the GraFix-ed hSARM1^{E642Q} map (colored as in Figure 2A).

Two neighboring ARM domains (yellow) are outlined by a black line and the NAD+ binding cleft of

a TIR domain that is bound to the two ARMs is highlighted in green. The interfaces formed

between the TIR and ARMs are designated as the 'primary TIR docking site' and the 'secondary

678 TIR docking site'. B) Two 'open-book' representations (in the same orientation) of the 'primary

679 TIR docking site'. Left – the TIR and ARM domains are colored as in (A), and the interface

680 surfaces in gray are encircled by green dashed line. Site-directed mutagenesis sites are

681 indicated. Right - amino acid conservation at the 'primary TIR docking site'. Cyan through maroon

682 are used to indicate amino acids, from variable to conserved, demonstrating an overall high level

683 of conservation in this interface. C) Toxicity of the hSARM1 construct and mutants in HEK293T

684 cells. The cells were transfected with hSARM1 expression vectors, as indicated. Cell viability was

685 measured and quantified 24 h post-transfection using the fluorescent resazurin assay. While cell

686 viability is virtually unaffected after 24 hr by ectopic expression of hSARM1$^{w.t.}$ and hSARM1^{E642Q},

687 deletion of the inhibiting ARM domain (which results in the SAM$^{1–2}$–TIR construct) induces

688 massive cell death. Mutations at the 'primary TIR docking site' of the ARM domain also induce

689 cell death, similar to the 'delARM' construct (three biological repeats, Student t test; ∗∗∗ $p < 0.001$;

690 ∗ $p < 0.05$; n.s: no significance). D) Kinetic measurement of purified hSARM1 NADase activity.

691 *Km* and *Vmax* were determined by fitting the data to the Michaelis-Menten equation and are

692 presented as mean ± SEM for three independent measurements.

693 E) HPLC analysis of time dependent NAD+ consumption (50µM) by hSARM1, and further

694 activation by NMN (0.2 and 1 mM). Time points 0 (black), 5 (green), and 30 (red) minutes. Right

695 graph shows the rate of ADPR product generation: no NMN (green), 0.2mM NMN (orange), 1mM

696 NMN (red). While 0.2mM NMN has no visible effect, 1mM NMN increases hSARM1 activity by

697 ~30%.

698 F) Glycerol inhibition of hSARM1 NADase *in vitro* activity was measured 20 minutes after adding

699 0.5µM NAD+ to the reaction mixture. In the same way, hSARM1^{E642Q} activity was measured and

700 compared to that of hSARM1$^{w.t.}$, showing attenuated NADase activity of the former.

701

Figure 4

A

B

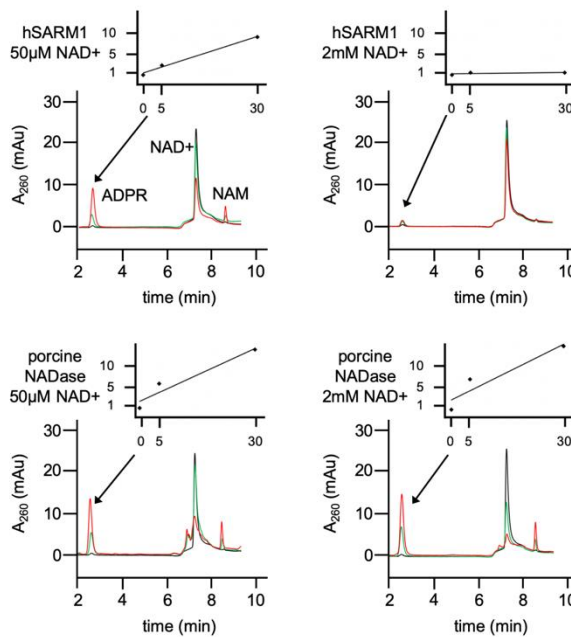

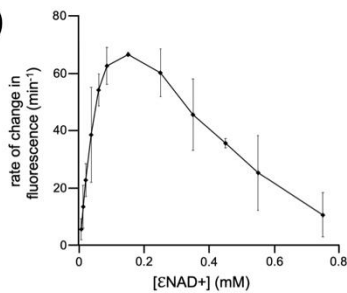no supplement

+ 10mM ATP

+ 5mM NAD+

C

D

E
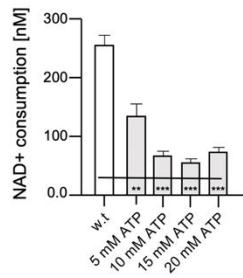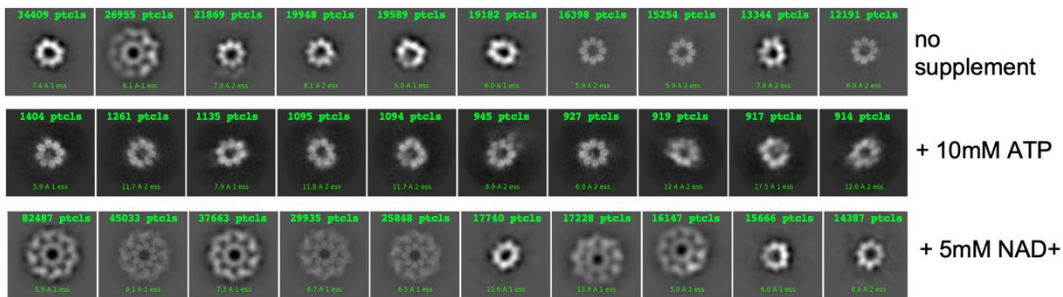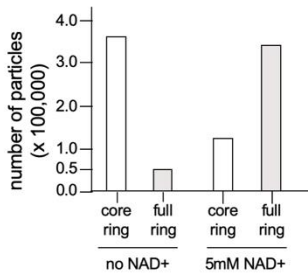
702

703 Figure 4. NAD+ induces structural and enzymatic inhibition of hSARM1

704 A) Inhibition of hSARM1 NADase activity by ATP was demonstrated and analyzed as in Figure

705 3F. B) The structural effects of NAD+ and ATP were observed by cryo-EM based on appearance

706 in 2D classification. Presented are the 10 most populated classes (those with the largest number

707 of particles – numbers in green, 1st class is on the left) out of 50-100 from each data collection

708 after the first round of particle picking and classification. By this analysis, the percentage of
709 particles that present full, two-ring structure is 13% (no NAD+); 74% (5mM NAD+); and 4%
710 (10mM ATP). C) Total number of particles with full ring assembly vs. those where only the inner
711 ring is visible. Conditions of sample preparation, freezing, collection, and processing were
712 identical, except for the NAD+ supplement in one of the samples. D) Rate of change in nucleotide
713 fluorescence under steady-state conditions of eNAD hydrolysis by hSARM1. Reactions were
714 initiated by mixing 400nM enzyme with different concentrations of 1:10 eNAD+:NAD+ (mol/mol)
715 mixtures. Three repeats, standard deviation error bars. E) HPLC analysis of time dependent
716 NAD+ consumption by hSARM1 and porcine brain NADase control in 50μM and 2mM. Time
717 points 0 (black), 5 (green), and 30 (red) minutes. Inset graph shows the rate of ADPR product
718 generation. While the rate of NAD+ hydrolysis by porcine NADase is maintained through 50μM
719 and 2mM NAD+, hSARM1 is tightly inhibited by 2mM NAD+.
720

Figure 5

A
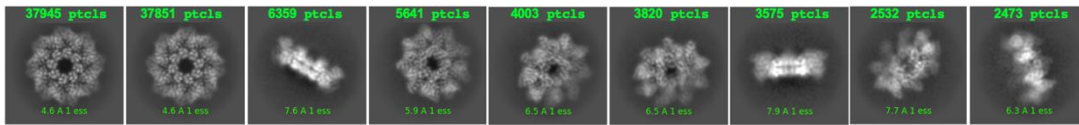
B

+5mM NAD+ top view   bottom view   side view

C
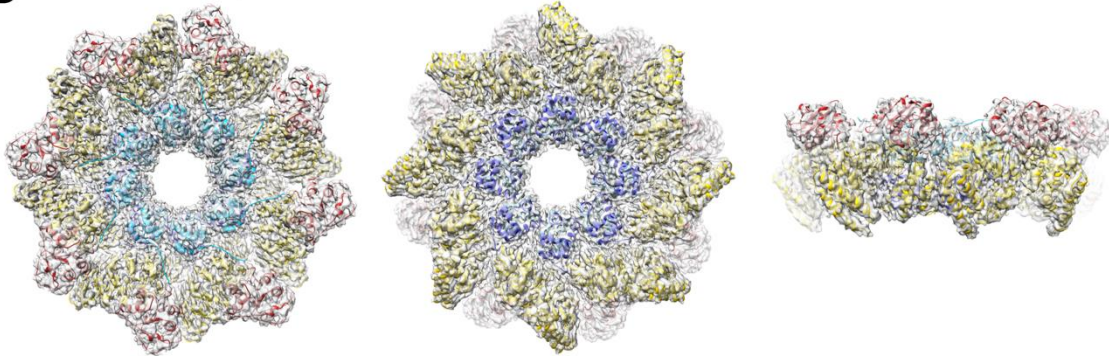
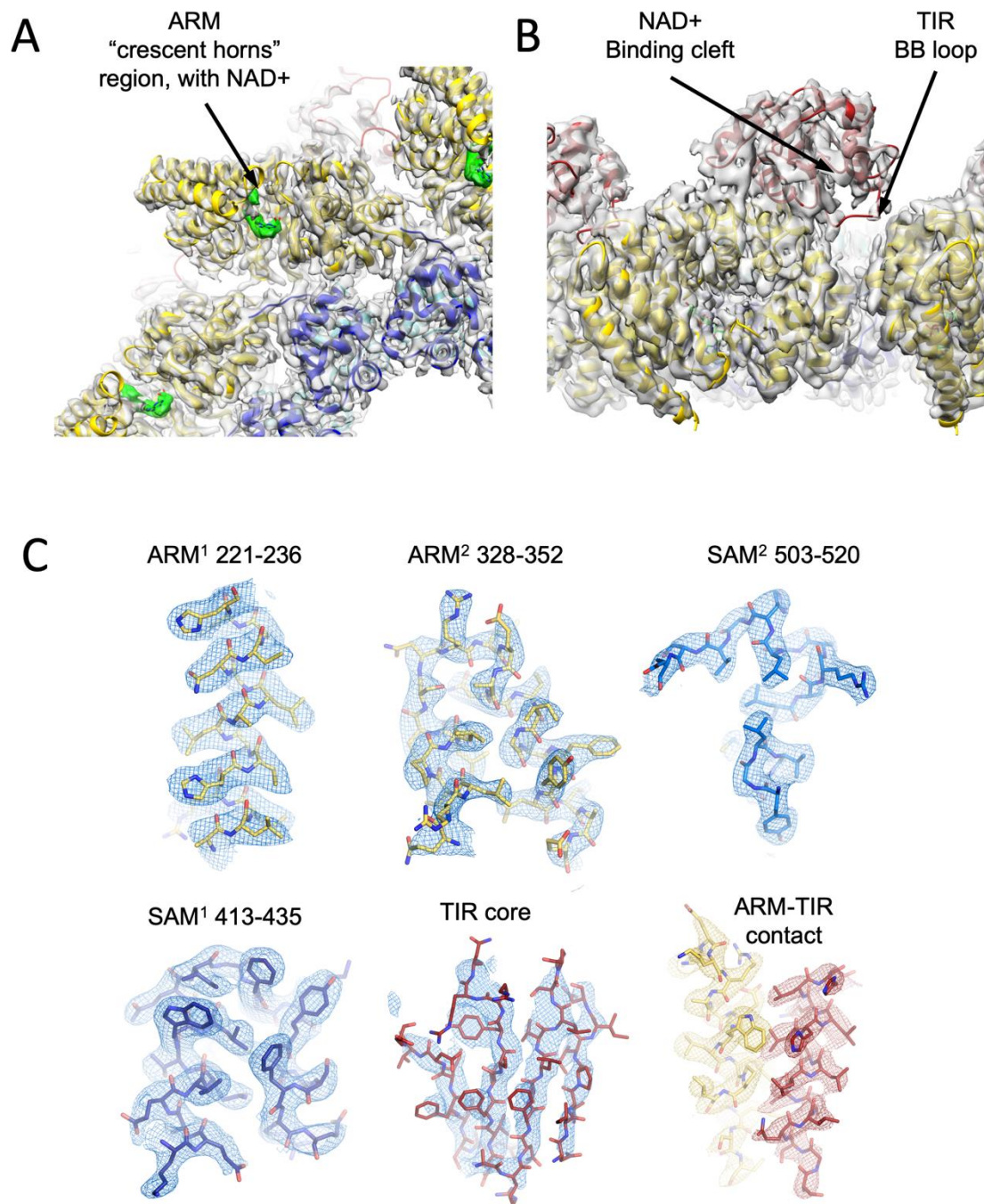GraFix, w/o NAD+   5mM NAD+, w/o GraFix
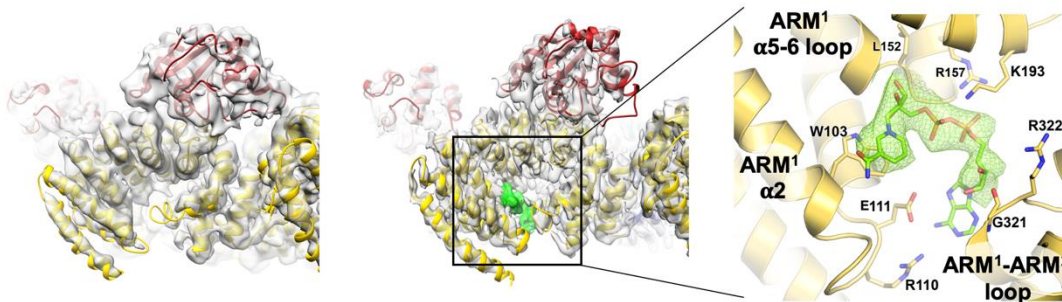
D
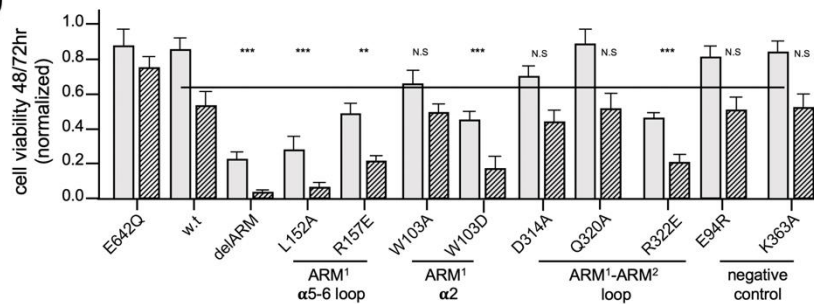
721

722 Figure 5. 3D structure reveals an inhibitory ARM allosteric NAD+ binding site.

723 A) Selected representation of 2D class averages used for the 3D reconstruction of

724 hSARM1^{E642Q} supplemented with 5mM of NAD+. The number of particles that were

725 included in each class average are indicated. B) Color coded (as in Figure 1A) protein

726 model docked in a transparent 2.7 Å cryo-EM density map (gray). C) When compared to
727 the GraFix-ed map, without NAD+ supplement (left), an extra density appears at the
728 'ARM horns' region in the NAD+ supplemented map (middle, right). The extra density is
729 rendered in green and an NAD+ molecule is fitted to it. The NAD+ is surrounded by three
730 structural elements, as indicated on the right panel. The NAD+ directly interacts with the
731 surrounding residues: the nicotinamide moiety is stacked onto the W103 sidechain rings;
732 the following ribose with L152 and H190; R110 form salt bridge with phosphate alpha
733 (proximal to the nicotinamide), while the beta phosphate (distal to the nicotinamide) form
734 salt bridges with R110 and R157. The map density at the distal ribose and adenosine
735 moieties is less sharp, but clearly involves interactions with the ARM^2 R322, G323 and
736 D326. In this way, activation by NMN, that lacks the distal phosphate, ribose and
737 adenosine, can be explained by binding to ARM^1 while preventing the bridging
738 interactions with ARM^2. D) Toxicity of the hSARM1 construct and mutants in HEK293F
739 cells. The cells were transfected with hSARM1 expression vectors, as indicated. Viable
740 cells were counted 48 (bars in gray) and 72 (bars in black stripes) hours post-
741 transfection. Moderate reduction in cell viability due to ectopic expression of hSARM1$^{w.t.}$
742 becomes apparent 72 hours after transfection, when compared with the NADase
743 attenuated hSARM1^{E642Q}, while the 'delARM' construct marks a constitutive activity that
744 brings about almost complete cell death after three days. Mutations at the ARM^1 α5-6
745 and ARM^1-ARM^2 loops induce cell death at a similar level as the 'delARM' construct,
746 while the control mutations and W103A did not show increased activity (three biological
747 repeats, Student t test; ∗∗∗ $p < 0.001$; ∗ $p < 0.05$; n.s: no significance).
748

A — ARM "crescent horns" region, with NAD+

B — NAD+ Binding cleft; TIR BB loop

C

ARM[1] 221-236

ARM[2] 328-352

SAM[2] 503-520

SAM[1] 413-435

TIR core

ARM-TIR contact

749

750

751 Figure 5 - Figure supplement 1. Cartoon model and density map (in transparent gray) of the

752 NAD+ supplemented hSARM1. Color code is as in Fig. A1. A) A zoom-in bottom view with

753 indication of the 'ARM horns' region. NAD+ densities are in green. Note the ARM domain

754 interactions with neighboring SAM and ARM domains. B) A zoom-in view of the TIR domain
755 docking onto two neighboring ARM domains. The NAD+ binding cleft and BB loop are indicated.
756 C) Density map (in mesh) showing a close-up view of isolated segments of the ARM, SAM and
757 TIR sections. The backbone and side chains are represented as sticks and colored in yellow,
758 blue, and red, respectively, as in Fig. 1A.
759

760
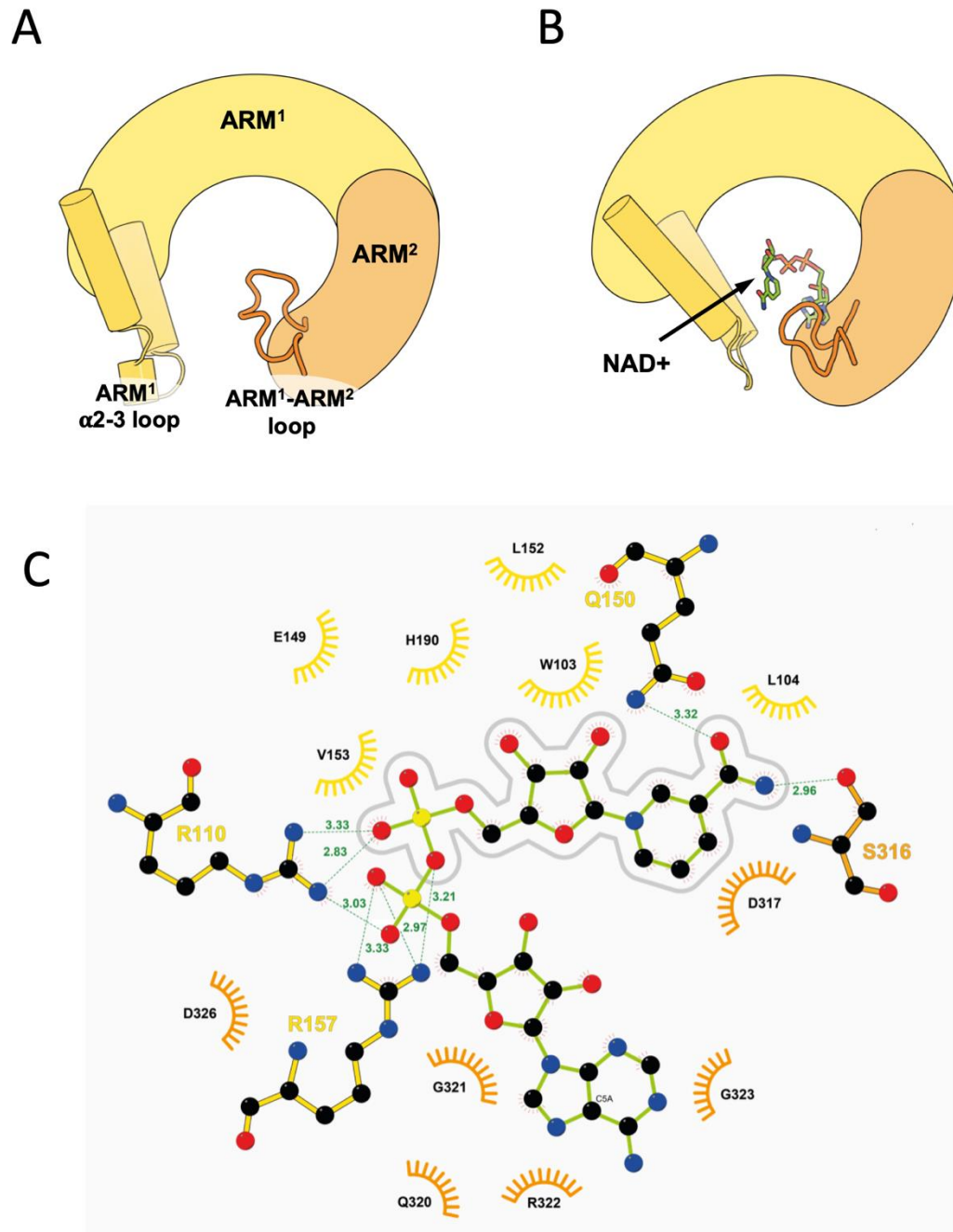
Figure 5 - Figure supplement 2. Zooming-in on the ARM allosteric NAD+ binding site.

A, B) The principle structural rearrangements in the ARM domain are presented as simplify
illustration based on a comparison between the GraFix-ed (A) and the NAD+ supplemented (B)
SARM1 cryo-EM maps. The ARM[1] and ARM[2] subdomains are depicted in yellow and orange,
respectively, and the ARM[1] α2-3 loop and ARM[1] and ARM[2] are highlighted. C) 2D Ligplot

766 (Wallace et al., 1995) diagram details the hydrogen bonds, salt bridges and hydrophobic
767 interactions between NAD+ and SARM1, where ARM[1] residues are colored in yellow, and ARM[2]
768 residues - in orange. The NMN moiety of NAD+ is outlined by a gray line drawing. According to
769 this analysis, the NMN moiety mostly interacts (but not only) with ARM[1] residues: W103, L104,
770 E149, Q150, L152, V153, H190, and has a partial interaction with R110. S316 and D317 of ARM[2]
771 also interact with the NMN moiety. The adenosine half of NAD+ mostly interacts (but not only)
772 with ARM[2] residues: Q320, G321, R322, G323, and D326. R110 and R157 of ARM[1] also interact
773 with the adenosine half.
774
775

Figure 6
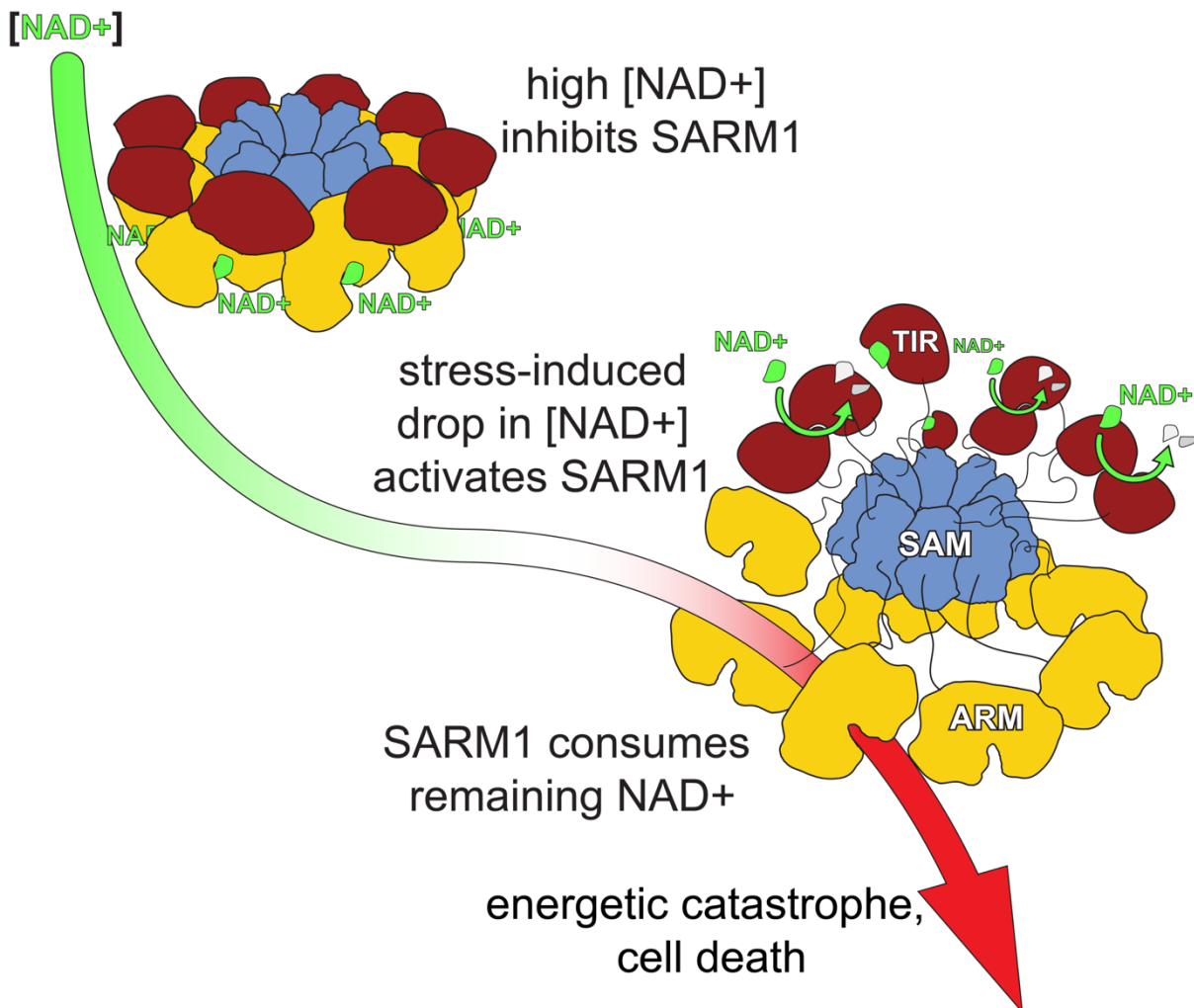
Figure 6. A model for hSARM1 inhibition and activation.
In homeostasis, the cellular NAD+ concentration is high enough and binds to an allosteric site that drives hSARM1 compact conformation. In this conformation, the catalytic TIR domains (red) are docked on ARM domains (yellow) apart from each other, unable to form close dimers required for NAD+ catalysis. When cellular NAD+ levels drop as a result of reduced NAD+

782 synthesis (e.g. inhibition of NMNAT1/2) or increased NAD+ consumption, the inhibiting NAD+
783 molecules fall off hSARM1, leading to the disintegration of the ARM-TIR outer ring assembly. Still
784 held by the constitutively-assembled SAM inner ring, the now-released TIR domains are at a high
785 local concentration that facilitates their dimerization and ensued NADase activity. When released
786 from allosteric inhibition, hSARM1 is only subjected to competitive inhibition such as by its
787 products ADPR and NAM, which are not found in high enough concentrations to block its activity
788 entirely. This leads to an almost complete consumption of the NAD+ cellular pool and to an
789 energetic catastrophe from which there may be no return.
790

791
792
793

794 Ashkenazy, H., Abadi, S., Martz, E., Chay, O., Mayrose, I., Pupko, T., and Ben-Tal, N.
795 (2016). ConSurf 2016: an improved methodology to estimate and visualize evolutionary
796 conservation in macromolecules. Nucleic Acids Res *44*, W344-350.
797 Bratkowski, M., Xie, T., Thayer, D.A., Lad, S., Mathur, P., Yang, Y.S., Danko, G., Burdett,
798 T.C., Danao, J., Cantor, A.*, et al.* (2020). Structural and Mechanistic Regulation of the Pro-
799 degenerative NAD Hydrolase SARM1. Cell reports *32*, 107999.
800 Cambronne, X.A., Stewart, M.L., Kim, D., Jones-Brunette, A.M., Morgan, R.K., Farrens,
801 D.L., Cohen, M.S., and Goodman, R.H. (2016). Biosensor reveals multiple sources for
802 mitochondrial NAD(+). Science *352*, 1474-1477.
803 Carty, M., Goodbody, R., Schroder, M., Stack, J., Moynagh, P.N., and Bowie, A.G. (2006).
804 The human adaptor SARM negatively regulates adaptor protein TRIF-dependent Toll-like
805 receptor signaling. Nat Immunol *7*, 1074-1081.
806 Chuang, C.F., and Bargmann, C.I. (2005). A Toll-interleukin 1 repeat protein at the synapse
807 specifies asymmetric odorant receptor expression via ASK1 MAPKKK signaling. Genes Dev
808 *19*, 270-281.
809 Coleman, M.P., and Hoke, A. (2020). Programmed axon degeneration: from mouse to
810 mechanism to medicine. Nat Rev Neurosci *21*, 183-196.
811 Couillault, C., Pujol, N., Reboul, J., Sabatier, L., Guichou, J.F., Kohara, Y., and Ewbank, J.J.
812 (2004). TLR-independent control of innate immunity in Caenorhabditis elegans by the TIR
813 domain adaptor protein TIR-1, an ortholog of human SARM. Nat Immunol *5*, 488-494.
814 Di Stefano, M., Nascimento-Ferreira, I., Orsomando, G., Mori, V., Gilley, J., Brown, R.,
815 Janeckova, L., Vargas, M.E., Worrell, L.A., Loreto, A.*, et al.* (2015). A rise in NAD
816 precursor nicotinamide mononucleotide (NMN) after injury promotes axon degeneration.
817 Cell death and differentiation *22*, 731-742.
818 Emsley, P., Lohkamp, B., Scott, W.G., and Cowtan, K. (2010). Features and development of
819 Coot. Acta Cryst D *66*, 486-501.
820 Essuman, K., Summers, D.W., Sasaki, Y., Mao, X., DiAntonio, A., and Milbrandt, J. (2017).
821 The SARM1 Toll/Interleukin-1 Receptor Domain Possesses Intrinsic NAD(+) Cleavage
822 Activity that Promotes Pathological Axonal Degeneration. Neuron *93*, 1334-1343 e1335.
823 Essuman, K., Summers, D.W., Sasaki, Y., Mao, X., Yim, A.K.Y., DiAntonio, A., and
824 Milbrandt, J. (2018). TIR Domain Proteins Are an Ancient Family of NAD(+)-Consuming
825 Enzymes. Curr Biol *28*, 421-430 e424.
826 Figley, M.D., and DiAntonio, A. (2020). The SARM1 axon degeneration pathway: control of
827 the NAD(+) metabolome regulates axon survival in health and disease. Current opinion in
828 neurobiology *63*, 59-66.
829 Geisler, S., Doan, R.A., Strickland, A., Huang, X., Milbrandt, J., and DiAntonio, A. (2016).
830 Prevention of vincristine-induced peripheral neuropathy by genetic deletion of SARM1 in
831 mice. Brain *139*, 3092-3108.
832 Geisler, S., Huang, S.X., Strickland, A., Doan, R.A., Summers, D.W., Mao, X., Park, J.,
833 DiAntonio, A., and Milbrandt, J. (2019). Gene therapy targeting SARM1 blocks pathological
834 axon degeneration in mice. J Exp Med *216*, 294-303.
835 Gerdts, J., Brace, E.J., Sasaki, Y., DiAntonio, A., and Milbrandt, J. (2015). SARM1
836 activation triggers axon degeneration locally via NAD(+) destruction. Science *348*, 453-457.
837 Gerdts, J., Summers, D.W., Milbrandt, J., and DiAntonio, A. (2016). Axon Self-Destruction:
838 New Links among SARM1, MAPKs, and NAD+ Metabolism. Neuron *89*, 449-460.
839 Gerdts, J., Summers, D.W., Sasaki, Y., DiAntonio, A., and Milbrandt, J. (2013). Sarm1-
840 mediated axon degeneration requires both SAM and TIR interactions. J Neurosci *33*, 13569-
841 13580.

842   Gilley, J., Orsomando, G., Nascimento-Ferreira, I., and Coleman, M.P. (2015). Absence of
843   SARM1 rescues development and survival of NMNAT2-deficient axons. Cell reports *10*,
844   1974-1981.
845   Hara, N., Osago, H., Hiyoshi, M., Kobayashi-Miura, M., and Tsuchiya, M. (2019).
846   Quantitative analysis of the effects of nicotinamide phosphoribosyltransferase induction on
847   the rates of NAD+ synthesis and breakdown in mammalian cells using stable isotope-labeling
848   combined with mass spectrometry. PLoS One *14*, e0214000.
849   Horsefield, S., Burdett, H., Zhang, X., Manik, M.K., Shi, Y., Chen, J., Qi, T., Gilley, J., Lai,
850   J.S., Rank, M.X.*, et al.* (2019). NAD(+) cleavage activity by animal and plant TIR domains
851   in cell death pathways. Science *365*, 793-799.
852   Hou, Y.J., Banerjee, R., Thomas, B., Nathan, C., Garcia-Sastre, A., Ding, A., and Uccellini,
853   M.B. (2013). SARM is required for neuronal injury and cytokine production in response to
854   central nervous system viral infection. J Immunol *191*, 875-883.
855   Houtkooper, R.H., Canto, C., Wanders, R.J., and Auwerx, J. (2010). The secret life of
856   NAD+: an old metabolite controlling new metabolic signaling pathways. Endocr Rev *31*,
857   194-223.
858   Jiang, Y., Liu, T., Lee, C.H., Chang, Q., Yang, J., and Zhang, Z. (2020). The NAD(+)-
859   mediated self-inhibition mechanism of pro-neurodegenerative Sarm1. Nature.
860   Kanamori, K.S., de Oliveira, G.C., Auxiliadora-Martins, M., Schoon, R.A., Reid, J.M., and
861   Chini, E.N. (2018). Two Different Methods of Quantification of Oxidized Nicotinamide
862   Adenine Dinucleotide (NAD. Bio Protoc *8*.
863   Kandiah, E., Giraud, T., de Maria Antolinos, A., Dobias, F., Effantin, G., Flot, D., Hons, M.,
864   Schoehn, G., Susini, J., Svensson, O.*, et al.* (2019). CM01: a facility for cryo-electron
865   microscopy at the European Synchrotron. Acta crystallographica Section D, Structural
866   biology *75*, 528-535.
867   Kastner, B., Fischer, N., Golas, M.M., Sander, B., Dube, P., Boehringer, D., Hartmuth, K.,
868   Deckert, J., Hauer, F., Wolf, E.*, et al.* (2008). GraFix: sample preparation for single-particle
869   electron cryomicroscopy. Nat Methods *5*, 53-55.
870   Kim, Y., Zhou, P., Qian, L., Chuang, J.Z., Lee, J., Li, C., Iadecola, C., Nathan, C., and Ding,
871   A. (2007). MyD88-5 links mitochondria, microtubules, and JNK3 in neurons and regulates
872   neuronal survival. J Exp Med *204*, 2063-2074.
873   Kingston, R.E., Chen, C.A., and Rose, J.K. (2003). Calcium phosphate transfection. Curr
874   Protoc Mol Biol *Chapter 9*, Unit 9.1.
875   Ko, K.W., Milbrandt, J., and DiAntonio, A. (2020). SARM1 acts downstream of
876   neuroinflammatory and necroptotic signaling to induce axon degeneration. J Cell Biol *219*.
877   Krauss, R., Bosanac, T., Devraj, R., Engber, T., and Hughes, R.O. (2020). Axons Matter: The
878   Promise of Treating Neurodegenerative Disorders by Targeting SARM1-Mediated Axonal
879   Degeneration. Trends Pharmacol Sci *41*, 281-293.
880   Krissinel, E. (2012). Enhanced fold recognition using efficient short fragment clustering. J
881   Mol Biochem *1*, 76-85.
882   Lebedev, A.A., Young, P., Isupov, M.N., Moroz, O.V., Vagin, A.A., and Murshudov, G.N.
883   (2012). JLigand: a graphical tool for the CCP4 template-restraint library. Acta Crystallogr D
884   Biol Crystallogr *68*, 431-440.
885   Li, C.C., and Lin, E.C. (1983). Glycerol transport and phosphorylation by rat hepatocytes. J
886   Cell Physiol *117*, 230-234.
887   Li, X., Mooney, P., Zheng, S., Booth, C.R., Braunfeld, M.B., Gubbens, S., Agard, D.A., and
888   Cheng, Y. (2013). Electron counting and beam-induced motion correction enable near-
889   atomic-resolution single-particle cryo-EM. Nature methods *10*, 584-590.

Liberati, N.T., Fitzgerald, K.A., Kim, D.H., Feinbaum, R., Golenbock, D.T., and Ausubel, F.M. (2004). Requirement for a conserved Toll/interleukin-1 resistance domain protein in the Caenorhabditis elegans immune response. Proc Natl Acad Sci U S A *101*, 6593-6598.

Liu, H.W., Smith, C.B., Schmidt, M.S., Cambronne, X.A., Cohen, M.S., Migaud, M.E., Brenner, C., and Goodman, R.H. (2018a). Pharmacological bypass of NAD(+) salvage pathway protects neurons from chemotherapy-induced degeneration. Proc Natl Acad Sci U S A *115*, 10654-10659.

Liu, L., Su, X., Quinn, W.J., 3rd, Hui, S., Krukenberg, K., Frederick, D.W., Redpath, P., Zhan, L., Chellappa, K., White, E.*, et al.* (2018b). Quantitative Analysis of NAD Synthesis-Breakdown Fluxes. Cell Metab *27*, 1067-1080 e1065.

Loring, H.S., Parelkar, S.S., Mondal, S., and Thompson, P.R. (2020). Identification of the first noncompetitive SARM1 inhibitors. Bioorg Med Chem *28*, 115644.

Martinez, M., Jimenez-Moreno, A., Maluenda, D., Ramirez-Aportela, E., Melero, R., Cuervo, A., Conesa, P., Del Cano, L., Fonseca, Y.C., Sanchez-Garcia, R.*, et al.* (2020). Integration of Cryo-EM Model Building Software in Scipion. J Chem Inf Model.

Mastronarde, D.N. (2005). Automated electron microscope tomography using robust prediction of specimen movements. Journal of structural biology *152*, 36-51.

Mink, M., Fogelgren, B., Olszewski, K., Maroy, P., and Csiszar, K. (2001). A novel human gene (SARM) at chromosome 17q11 encodes a protein with a SAM motif and structural similarity to Armadillo/beta-catenin that is conserved in mouse, Drosophila, and Caenorhabditis elegans. Genomics *74*, 234-244.

Mukherjee, P., Woods, T.A., Moore, R.A., and Peterson, K.E. (2013). Activation of the innate signaling molecule MAVS by bunyavirus infection upregulates the adaptor protein SARM1, leading to neuronal death. Immunity *38*, 705-716.

Murata, H., Khine, C.C., Nishikawa, A., Yamamoto, K.I., Kinoshita, R., and Sakaguchi, M. (2018). c-Jun N-terminal kinase (JNK)-mediated phosphorylation of SARM1 regulates NAD(+) cleavage activity to inhibit mitochondrial respiration. J Biol Chem *293*, 18933-18943.

Murata, H., Sakaguchi, M., Kataoka, K., and Huh, N.H. (2013). SARM1 and TRAF6 bind to and stabilize PINK1 on depolarized mitochondria. Mol Biol Cell *24*, 2772-2784.

Murshudov, G.N., Skubak, P., Lebedev, A.A., Pannu, N.S., Steiner, R.A., Nicholls, R.A., Winn, M.D., Long, F., and Vagin, A.A. (2011). REFMAC5 for the refinement of macromolecular crystal structures. Acta Cryst D *67*, 355-367.

Osterloh, J.M., Yang, J., Rooney, T.M., Fox, A.N., Adalbert, R., Powell, E.H., Sheehan, A.E., Avery, M.A., Hackett, R., Logan, M.A.*, et al.* (2012). dSarm/Sarm1 is required for activation of an injury-induced axon death pathway. Science *337*, 481-484.

Ozaki, E., Gibbons, L., Neto, N.G., Kenna, P., Carty, M., Humphries, M., Humphries, P., Campbell, M., Monaghan, M., Bowie, A.*, et al.* (2020). SARM1 deficiency promotes rod and cone photoreceptor cell survival in a model of retinal degeneration. Life Sci Alliance *3*.

Panneerselvam, P., Singh, L.P., Ho, B., Chen, J., and Ding, J.L. (2012). Targeting of pro-apoptotic TLR adaptor SARM to mitochondria: definition of the critical region and residues in the signal sequence. Biochem J *442*, 263-271.

Punjani, A., Rubinstein, J.L., Fleet, D.J., and Brubaker, M.A. (2017). cryoSPARC: algorithms for rapid unsupervised cryo-EM structure determination. Nature Methods *14*, 290-+.

Reed, M.C., Lieb, A., and Nijhout, H.F. (2010). The biological significance of substrate inhibition: a mechanism with diverse functions. Bioessays *32*, 422-429.

Sasaki, Y., Nakagawa, T., Mao, X., DiAntonio, A., and Milbrandt, J. (2016). NMNAT1 inhibits axon degeneration via blockade of SARM1-mediated NAD(+) depletion. Elife *5*.

939   Sporny, M., Guez-Haddad, J., Lebendiker, M., Ulisse, V., Volf, A., Mim, C., Isupov, M.N.,
940   and Opatowsky, Y. (2019). Structural Evidence for an Octameric Ring Arrangement of
941   SARM1. J Mol Biol *431*, 3591-3605.
942   Summers, D.W., DiAntonio, A., and Milbrandt, J. (2014). Mitochondrial dysfunction induces
943   Sarm1-dependent cell death in sensory neurons. J Neurosci *34*, 9338-9350.
944   Summers, D.W., Gibson, D.A., DiAntonio, A., and Milbrandt, J. (2016). SARM1-specific
945   motifs in the TIR domain enable NAD+ loss and regulate injury-induced SARM1 activation.
946   Proc Natl Acad Sci U S A *113*, E6271-E6280.
947   Sundaramoorthy, V., Green, D., Locke, K., O'Brien, C.M., Dearnley, M., and Bingham, J.
948   (2020). Novel role of SARM1 mediated axonal degeneration in the pathogenesis of rabies.
949   PLoS Pathog *16*, e1008343.
950   Tegunov, D., and Cramer, P. (2019). Real-time cryo-electron microscopy data preprocessing
951   with Warp. Nat Methods *16*, 1146-1152.
952   Uccellini, M.B., Bardina, S.V., Sanchez-Aparicio, M.T., White, K.M., Hou, Y.J., Lim, J.K.,
953   and Garcia-Sastre, A. (2020). Passenger Mutations Confound Phenotypes of SARM1-
954   Deficient Mice. Cell reports *31*, 107498.
955   Vagin, A., and Teplyakov, A. (2010). Molecular replacement with MOLREP. Acta Cryst D
956   *66*, 22-25.
957   Vagin, A.A., and Isupov, M.N. (2001). Spherically averaged phased translation function and
958   its application to the search for molecules and fragments in electron-density maps. Acta
959   Crystallogr D Biol Crystallogr *57*, 1451-1456.
960   Wallace, A.C., Laskowski, R.A., and Thornton, J.M. (1995). LIGPLOT: a program to
961   generate schematic diagrams of protein-ligand interactions. Protein Eng *8*, 127-134.
962   Winn, M.D., Ballard, C.C., Cowtan, K.D., Dodson, E.J., Emsley, P., Evans, P.R., Keegan,
963   R.M., Krissinel, E.B., Leslie, A.G., McCoy, A.*, et al.* (2011). Overview of the CCP4 suite
964   and current developments. Acta Cryst D *67*, 235-242.
965   Zhang, K. (2016). Gctf: Real-time CTF determination and correction. J Struct Biol *193*, 1-12.
966   Zhao, Z.Y., Xie, X.J., Li, W.H., Liu, J., Chen, Z., Zhang, B., Li, T., Li, S.L., Lu, J.G., Zhang,
967   L.*, et al.* (2019). A Cell-Permeant Mimetic of NMN Activates SARM1 to Produce Cyclic
968   ADP-Ribose and Induce Non-apoptotic Cell Death. iScience *15*, 452-466.
969